Check for updates

View Article Online
View Journal

Biomaterials Science

Accepted Manuscript

This article can be cited before page numbers have been issued, to do this please use: . IIK, D. Yucel and V. Hasirci, *Biomater. Sci.*, 2026, DOI: 10.1039/D5BM01824B.

ROYAL SOCIETY
OF CHEMISTRY

rsc.li/biomaterials-science

View Article Online
DOI: 10.1039/D5BM01824B

Modeling Hypoxia Integrated Glioblastoma Microenvironment to Mimic Tumor Heterogeneity and Chemoresistance

Seyma Isik[1,5], *Deniz Yücel*[1,2,4,5**], *Vasif Hasirci*[3,4,5,6*]

[1] Department of Medical Biotechnology, Graduate School of Health Sciences, Acibadem University, 34752 İstanbul, Türkiye

[2] Department of Histology and Embryology, School of Medicine, Acibadem University, 34752 İstanbul, Türkiye

[3] Department of Biomedical Engineering, Faculty of Engineering and Natural Sciences, Acibadem University, 34752 İstanbul, Türkiye

[4] Department of Biomaterials, Graduate School of Natural and Applied Sciences, Acibadem University, 34752 İstanbul, Türkiye

[5] Biomaterials Application and Research Center, Acibadem University, 34752 İstanbul, Türkiye

[6] BIOMATEN, Center of Excellence in Biomaterials and Tissue Engineering, Middle East Technical University, 06800 Ankara, Türkiye

* Corresponding author: vhasirci@metu.edu.tr

** Co-corresponding author: deniz.yucel@acibadem.edu.tr

ABSTRACT

Glioblastoma (GBM) is a highly aggressive brain tumor in which hypoxia plays a central role in driving tumor progression, cellular plasticity, and resistance to treatment. In order to mimic these pathological features under *in vitro* conditions, a bioprinted GBM model was developed by integrating a PDMS based hypoxia chip with a hydrogel composed of hyaluronic acid methacrylate (HAMA) and decellularized extracellular matrix (dECM), aiming to replicate the biochemical, mechanical, and oxygen deprived conditions of native tumors. Glioblastoma (U87) and microglia (HMC3) cells were bioprinted with the hydrogel into the core and the periphery of the compartmentalized model, respectively. Hypoxic conditions were generated passively through a barrier and monitored by a fluorescence based probe. The model was able to reproduce the key GBM features, including pseudopalisading necrosis (central Ki67$^-$/necrotic and peripheral Ki67$^+$/proliferative cells) and a 32% increase in invasion distance under hypoxic conditions. Gene expression analysis revealed hypoxic conditions induced the upregulation of proliferation (EGFR, Ki67), stemness (SOX2, NES), and invasion (MMP2) associated markers, while proteomic analysis showed increased glycolysis, HIF1 signaling, and amino acid biosynthesis. Drug testing with temozolomide (TMZ) demonstrated reduced sensitivity under hypoxic conditions, evidenced by a 56% increase in IC$_{50}$, reflecting clinically relevant therapy resistance. These findings showed the ability of the model to mimic key

View Article Online
DOI: 10.1039/D5BM01824B

properties of the GBM microenvironment at both phenotypic and molecular levels and offers a physiologically relevant platform to study GBM biology and evaluate therapeutic responses.

Keywords: Glioblastoma, Hypoxia, *In Vitro* Model, 3D Bioprinting, Therapy Resistance, IC_{50}

1. Introduction

Glioblastoma (GBM) is the most aggressive primary brain tumor in the central nervous system, characterized by rapid progression, high invasiveness, and resistance to standard treatments (1). Hypoxia is a characteristic feature of GBM tumor microenvironment (TME), contributing to tumor heterogeneity and therapeutic resistance. Under hypoxic conditions, stabilization of hypoxia inducible factors (HIFs) drives tumor adaptation by promoting metabolic reprogramming toward glycolysis and inducing phenotypic changes. HIF activation leads to resistance to chemotherapy and radiotherapy by inhibiting apoptotic pathways and activating cellular stress responses (2, 3). Hypoxia induced phenotypic shifts into the mesenchymal subtype further drive tumor aggressiveness and complicate therapeutic management, contributing to the poor prognosis of GBM (4).

Differences in oxygen availability cause spatial heterogeneity in GBM, resulting in distinct tumor compartments with specific roles in disease progression and resistance to therapy. Necrotic cores develop under severe hypoxia due to poor vascularization, leading to cell death and release of proinflammatory signals that promote tumor growth and invasion into surrounding healthy tissue. Pseudopalisading regions, although exhibiting increased vascularization, remain relatively hypoxic, which promotes an aggressive tumor phenotype, increases invasive subpopulations, and contributes to resistance to standard therapies (5-7).

Despite standard-of-care treatments including surgery, radiotherapy, and chemotherapy with temozolomide, GBM remains incurable. TME drives therapeutic resistance through interplay of cellular and extracellular components, hypoxic regions, and metabolic adaptations, that impair anti-tumor immunity and reduce sensitivity to temozolomide (8, 9). Many therapeutic approaches that show promise in preclinical studies fail in clinical trials. This is largely because conventional preclinical models, relying on 2D cell cultures followed by animal studies, cannot reflect the complexity and heterogeneity of the GBM microenvironment, limiting their predictive value for drug screening. Given that no single *in vitro* platform can fully mimics these microenvironmental features, models recapitulating specific physiological properties of native tumors may provide useful tools for studying disease mechanisms and drug development.

View Article Online
DOI: 10.1039/D5BM01824B

Several advanced *in vitro* models have been developed to reproduce pathological and microenvironmental features of GBM tumors, including hypoxia mimicking platforms (10-13), ECM-mimetic constructs (14, 15), and immune integrated tumor models (16-18).

The present study builds on these approaches by integrating hypoxic gradient, GBM-microglia interactions, and biomimetic extracellular matrix properties within a compartmentalized model. Although these microenvironmental interactions collectively drive GBM progression and therapeutic resistance, they have not been simultaneously represented within a single *in vitro* platform. For this purpose, U87 glioblastoma and HMC3 microglia cells were incorporated into a decellularized extracellular matrix (dECM) and hyaluronic acid methacrylate (HAMA) based bioink and bioprinted into a compartmentalized disc shaped structure. The dECM/HAMA-based bioink was formulated to mimic the compositional, mechanical, and rheological properties of native GBM tissue. In the PDMS chip system, central hypoxia was induced using a gas diffusion barrier. The platform reproduces several pathological features of GBM, including pseudopalisading necrosis, ECM remodeling, metabolic adaptation, and reduced temozolomide sensitivity, offering a physiologically relevant system for disease modeling and preclinical drug evaluation.

2. Materials and Methods

2.1. Materials

Human glioblastoma cell line U87 (ATCC: HTB-14, RRID: CVCL_0022) and human microglial cell line HMC3 (ATCC: CRL-3304, RRID: CVCL_II76) were gifted by scientists at Koc University and Ege University, respectively. Hyaluronic acid sodium salt from Streptococcus equi (#53747), 2-Hydroxy-4′-(2-hydroxyethoxy)-2-methylpropiophenone (#410896), Triton X-100 (#T8787) were purchased from Sigma Aldrich (USA). 4′,6-diamidino-2-phenylindole (#D21490), AlexaFluor 488-phalloidin (#A12379), RevertAid First Strand cDNA Synthesis Kit (#K1622), TRIzol reagent (#15596026) were obtained from ThermoScientific (USA). Fetal bovine serum (FBS) (#04-007-1A) was obtained from Sartorius Biological Industries (Israel). Phosphate buffered saline (PBS) without Ca+2 and Mg+2 (#14190-094), Opti-MEM Reduced Serum Medium (#31985062), high glucose Dulbecco's Modified Eagle's medium (#11965092), high glucose Dulbecco's Modified Eagle's medium phenol red free (#31053028), Normal Goat Serum (#PCN5000), penicillin/streptomycin (#15140-122), Trypsin-EDTA (#25200056) were purchased from Gibco (USA). PBS with Ca+2, Mg+2 (#PBS-2A) was obtained from Capricorn (Germany). Rabbit anti-human anti-

View Article Online
DOI: 10.1039/D5BM01824B

Ki67 IgG primary antibody (#ab15580) was purchased from Abcam (UK). AlamarBlue Cell Viability Reagent (#DAL1025), image IT green hypoxia reagent (#I14834), Lipofectamine 2000 Transfection Reagent (#11668019), LIVE/DEAD™ Viability/Cytotoxicity Kit (#L3224), Goat anti-Rabbit IgG (H+L) Cross-Adsorbed Secondary Antibody, Alexa Fluor™ 555 (#A-21428), Goat anti-Chicken IgY (H+L) Secondary Antibody, Alexa Fluor™ 488 (#A-11039), Chicken anti-human GFAP IgY (#PA1-10004) were purchased from Invitrogen (USA). pcDNA3-EGFP plasmid (#13031) was purchased from Addgene (USA). Ultra low attachment microplates (#10023683) were purchased from Corning (USA). SYLGARD™ 184 Silicone Elastomer Kit (#4019862) was obtained from Dow Chemical Company (USA). Direct-zol RNA miniprep (#R2051) was purchased from Zymo Research (USA). The primer sequences were designed based on gene sequences from the National Library of Medicine (NCBI) database and synthesized by Sentromer DNA Technologies (Türkiye). PowerUp™ SYBR™ Green Master Mix (#A25741) was obtained from Applied Biosystems (USA). Temozolomide (#sc203292) was purchased from Santa Cruz Biotecnology (USA). Fluorescein-sodium (0.4 kDa, #J61549) was obtained from Alfa Aesar (Germany).

2.2. Printability analysis of hydrogel solutions

Photoinitiator Irgacure 2959 was dissolved (3 mg/mL in 100 mL DMEM) at 37°C and subsequently cooled to 4°C. HAMA (1 g, 54% methacrylated form of hyaluronic acid sodium salt from Streptococcus equi) (19) was added to this solution and stirred overnight at 4°C. A powder of dECM (30 mg) was then added to the HAMA mixture (1 mL) and stirred overnight at 4°C. Rheological properties were measured at 10°C using a rheometer (Kinetux, Malvern, United Kingdom) equipped with a cone plate geometry. Shear thinning behavior was assessed by recording viscosity over a logarithmic shear rate range from 0.1 to 100 s^{-1}. Thixotropic behavior was analyzed using a three step shear protocol in which viscosity was first measured at rest (1 s^{-1} for 30 s), then under high shear to simulate extrusion (100 s^{-1} for 30 s), followed by recovery at low shear (1 s^{-1} for 60 s). Hydrogel solutions were loaded into syringes (nozzle 25G) and printed with a 3D printer (EnvisionTec 3D Bioplotter Developer Series, Germany). Constructs with internal patterns in honeycomb (hexagonal) and grid (rectangular) geometries were printed to assess printability. Printing parameters were set to be the pressure of 0.4 bar, cartridge movement speed of 10 mm/s, and cartridge temperature of 10°C. After printing, crosslinking was carried out under UV light (365 nm, 0.160 joule/cm^2).

View Article Online
DOI: 10.1039/D5BM01824B

2.3. Cell culture

Human glioblastoma (U87) and human microglial (HMC3) cells were cultured in tissue culture flasks with complete medium, high glucose Dulbecco's Modified Eagle's medium (DMEM) supplemented with 10% fetal bovine serum, and 1% penicillin/streptomycin. Cells were incubated in an incubator (37°C, 5% CO_2) with the medium replaced every two days. Upon reaching approximately 80% confluence, cells were detached using 0.25% trypsin-EDTA at 37°C for 5 min, centrifuged at 1500 rpm for 5 min, and the resulting pellet was resuspended in the hydrogel solution for subsequent experiments.

2.4. Transfection of U87 cells with the EGFP gene for live cell imaging

U87 cells were transfected with the Enhanced Green Fluorescent Protein (EGFP) gene using the pcDNA3-EGFP plasmid to enable live cell imaging in the co-culture model. Cells were seeded in 24 well plates and cultured for 18 h. A DNA-lipid complex was prepared by diluting 0.5 µg plasmid DNA and 2 µL Lipofectamine 2000 separately in 50 µL Opti-MEM, incubating each for 5 min, then combining and incubating for 20 min more. The mixture was added to each well, and the final volume adjusted to 1 mL with Opti-MEM. After 48 h, stably transfected cells (U87-EGFP) were selected using G418 (550 µg/mL) for 21 days, and EGFP expression was confirmed by fluorescence microscopy (Zeiss Axio Imager M2, Germany) and flow cytometry (BD Accuri C6 plus, USA).

2.5. 3D bioprinting of glioblastoma and microglia cells with HAMA/dECM bioink

HAMA/dECM solution (1%, w/v HAMA and 3% w/v dECM, 1H3D) was prepared in a beaker on a magnetic stirrer and kept on ice. U87 and HMC3 cells were detached from culture flasks through tripsinization, pelleted by centrifugation, and separately resuspended in hydrogel solutions to obtain Bioink 1 (U87, 10^7 cells/mL) and Bioink 2 (HMC3, 10^7 cells/mL). Each bioink was loaded into separate syringes of the EnvisionTEC 3D Bioplotter equipped with a 25 G nozzle. The printing parameters were set to be the pressure of 0.4 bar, cartridge movement speed of 10 mm/s, and cartridge temperature of 10°C, and dimensions of disc (9 mm diameter, 1 mm height). Bioink 1 was printed as a four layer inner region, followed by Bioink 2 printed around Bioink 1 (Fig. 1). Printed constructs were crosslinked under UV light (365 nm, 0.160 joule/cm^2, 2 min) and transferred to the center of the PDMS chip.

View Article Online
DOI: 10.1039/D5BM01824B

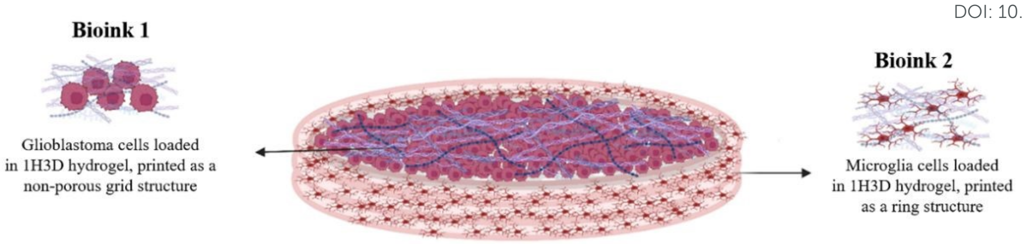

Figure 1. Scheme of 3D bioprinted model

2.6. Scanning electron microscopy (SEM) of the hydrogels

The cell free and cell loaded (bioprinted with glioblastoma and microglia cells and incubated for 7 days) dry hydrogels were examined using scanning electron microscopy (SEM). Firstly, the samples were washed with PBS (3 times, 5 min each), fixed with paraformaldehyde (4%, w/v) for 1 h, washed with PBS (3 times, 5 min each) and dH_2O. Then, fixed samples were frozen -80 °C overnight and lyophilized by freeze drying at -80°C. Dry hydrogels were coated with gold (20 Å, 120 s), and examined using a SEM (Zeiss EVO 10, Germany).

2.7. Live/Dead Assay

Viability of U87 and HMC3 co-culture in the bioprinted constructs was determined on days 1, 3, 7, and 14 using Live/Dead assay. Bioinks consisting of HAMA/dECM with U87 and HMC3 cells were prepared and bioprinted as described in Section 2.5, then incubated in a humidified incubator (37°C, 5% CO_2). Samples were washed with phenol red free DMEM (twice), stained with 2 µM calcein AM (live cells) and 4 µM ethidium homodimer-1 (EthD-1, dead cells) in phenol red free DMEM for 30 min at 37°C, then washed with phenol red free DMEM (twice), and examined with confocal laser scanning microscopy (CLSM, Zeiss LSM 900, Germany). Viability was quantified by counting live and dead cells using ImageJ (version 1.53k, NIH).

2.8. Production and characterization of the hypoxia chip

The hypoxia chip was fabricated from polydimethylsiloxane (PDMS; Sylgard 184) using a negative mold. A negative mold was produced using stereolithography (Formlabs Form 2, USA) with a light sensitive resin and printed at 45° angle. The printed molds were cleaned with isopropanol using ultrasonic cleaning for 30 min, then cured under 405 nm LED light at 60°C for 3 h. PDMS was prepared by mixing the elastomer base and curing agent at a 10:1 (v/v) ratio, then poured onto the negative molds, and cured in a vacuum oven at 70°C for 4 h (20). After curing, the PDMS chips (Fig. 2A) were removed from the molds, disinfected in 70% ethanol for 30 min, and sterilized by exposure to UV for 30 min each side. The PDMS chip was strongly

View Article Online
DOI: 10.1039/D5BM01824B

stuck to a glass slide by applying a thin layer of uncured PDMS between the surfaces and curing at 100°C for 1 h (Fig. 2B). The bioprinted, cell loaded hydrogel construct was positioned in the central chamber of the chip, and a glass slide was positioned over the hydrogels to prevent vertical oxygen diffusion (Fig. 2C, D). In the design, the glass slide served as an oxygen diffusion barrier, blocking atmospheric gas exchange and allowing oxygen entry only through the gas permeable PDMS side walls. Culture medium was supplied through the reservoirs and distributed via the side channels of the chip, allowing nutrient and drug transport predominantly by diffusion.

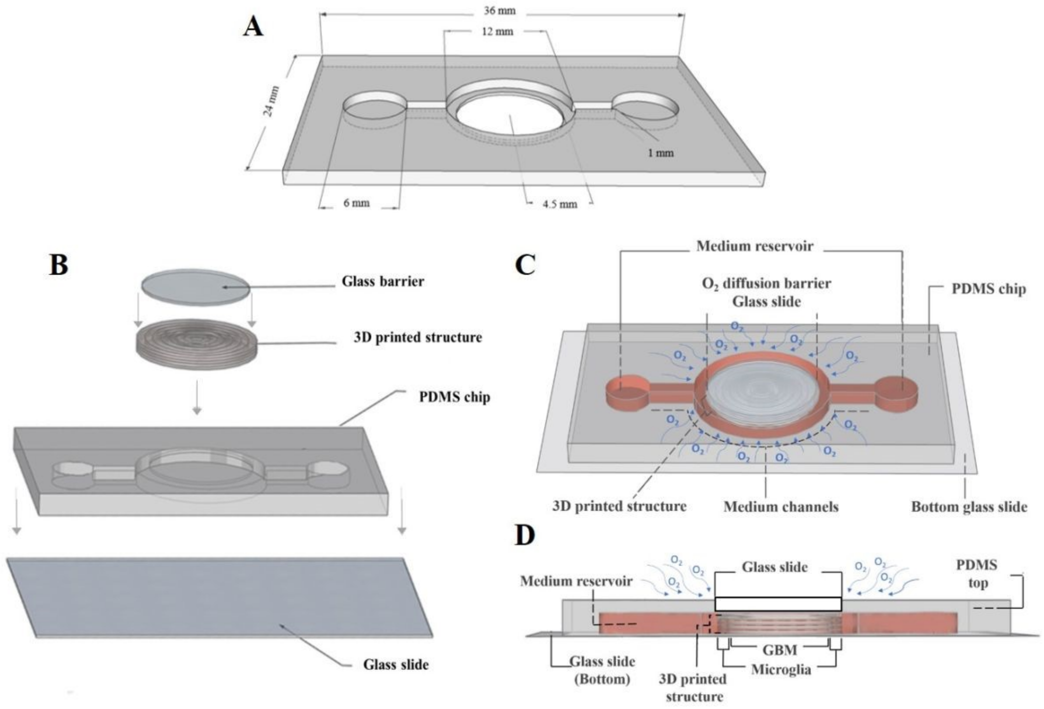

Figure 2. Scheme of hypoxia chips. (A) PDMS chip design. (C) Blow up of the chip. (C, D) Complete chip.

2.9. Staining of hypoxic cells

Central hypoxia was achieved by placing a glass slide over the hydrogel to block oxygen diffusion from the air. Cells were stained using Image-iT™ Green Hypoxia Reagent, which fluoresces when oxygen level is below 5%, increasing intensity under more severe hypoxia. After 72 h incubation in the hypoxia chip, the medium was replaced with fresh complete medium containing 5 μM Image-iT Green Hypoxia Reagent and incubated at 37°C for 3 h. Samples were then washed twice with PBS, incubated for 16 h, and examined using CLSM (Zeiss LSM 900, Germany). The images were acquired using same gain and laser power settings. Chips without the gas diffusion barrier served as normoxic controls. Image analysis

View Article Online
DOI: 10.1039/D5BM01824B

was performed using ImageJ (version 1.53k, NIH). Images were converted to 8-bit grayscale. Fluorescence intensity was quantified by measuring the Raw Integrated Density of equal sized fluorescence fields from images of three distinct regions, including center, intermediate, and periphery. Background fluorescence was corrected by subtracting the mean intensity of a non-fluorescent region multiplied by the corresponding measurement area. Brightness and contrast adjustments were applied equally across all images for visualization.

2.10. Detection of pseudopalisading regions using anti-Ki67 staining

Pseudopalisading regions in the hypoxia model were determined by anti-Ki67 immunofluorescence staining (21). After 7 days of incubation in the hypoxia chip, cells were fixed with paraformaldehyde (4%, w/v) for 15 min, washed with PBS (3 times, 5 in each), and permeabilized with Triton X-100 (0.1%, v/v in PBST) for 10 min. Nonspecific bindings were blocked with normal goat serum (5%, v/v in PBST) for 1 h. Cells were then washed with goat serum (1%, v/v in PBST) and incubated overnight at 4°C with primary antibody (rabbit anti-human Ki67 primary antibody, 1:1000, v/v in 1% goat serum). After washing with 1% goat serum (3 times, 5 min each), cells were incubated with secondary antibody (Alexa Fluor 555-conjugated anti-rabbit IgG secondary antibody, 1:500, v/v in 1% goat serum) and Alexa Fluor 488-phalloidin (1:200, v/v) at 37°C for 1 h. Samples were then washed with PBS (3 times, 5 min each) and examined using CLSM (Zeiss LSM 900, Germany). The images were acquired using same gain and laser power settings. Fluorescence intensity analysis was performed using ImageJ (version 1.53k, NIH). Images were converted to 8-bit grayscale. Regions of interest (ROIs) were manually drawn around individual Ki67-positive cells from images of three distinct regions, including center, intermediate, and periphery. For each ROI, the Raw Integrated Density was measured. Background was corrected by subtracting the mean intensity of a non-fluorescent region multiplied by the ROI area. Brightness and contrast adjustments were applied equally across all images for visualization.

2.11. Detection of necrotic regions using EthD-1 staining

Necrotic areas were identified by calcein and EthD-1 staining, after 7 days of incubation in the hypoxia chip. Samples were washed with phenol red free DMEM (twice), stained with 2 μM calcein AM (live cells, green) and 4 μM ethidium homodimer-1 (dead cells, red) in phenol red free DMEM for 30 min at 37°C, then washed with with phenol red free DMEM (twice), and imaged using CLSM (Zeiss LSM 900, Germany).

View Article Online
DOI: 10.1039/D5BM01824B

2.12. Analysis of gene expression in cells using real time polymerase chain reaction

Gene expression levels associated with GBM were analyzed using real time PCR (RT-PCR). Cells were cultured in the hypoxia chip for 7 days, while co-cultured cells grown on 2D monolayers, as well as those loaded in hydrogels under normoxic conditions, served as controls. Total RNA was extracted using the Direct-zol™ RNA Miniprep Kit according to the manufacturer’s protocol. Briefly, cell loaded hydrogels were homogenized in 1 mL TRIzol reagent by sonication (90 s, 10 s on/off), followed by the addition of 200 µL chloroform, incubation on ice for 15 min, and centrifugation (16,000 rpm, 15 min, 4°C) for phase separation. The aqueous phase was transferred to a new tube, mixed with an equal volume of absolute ethanol, and loaded onto Zymo-Spin™ IICR columns. Columns were washed with RNA Wash Buffer, treated with DNase I for 15 min, rinsed with Direct-zol™ RNA PreWash, and eluted in 50 µL DNase/RNase free water. RNA concentration and purity were determined using a Nanodrop spectrophotometer (Nanodrop 1/1, Thermo Fisher Scientific, USA). First strand cDNA was synthesized from 1 µg total RNA using the RevertAid First Strand cDNA Synthesis Kit with random primers, according to the manufacturer’s protocol, by incubating at 42°C for 60 min followed by 70°C for 5 min. RT-PCR was carried out with PowerUp™ SYBR™ Green Master Mix in 20 µL reactions containing 0.7 µM gene specific primers (Supplementary Table 1) and 50 ng cDNA, using a real-time PCR system (BioRad CFX 96, USA). Cycling conditions were: UDG activation at 50°C for 2 min, Dual-Lock™ DNA polymerase activation at 95°C for 2 min, followed by 40 cycles of 95°C for 15 s and 60°C for 1 min. Melting curve analysis was performed from 60 to 95°C. GAPDH served as the reference gene, and relative gene expression was calculated using the $2^{-\Delta\Delta Ct}$ method.

2.13. Proteomics Analysis using LC-MS/MS

Proteomic profiling was performed using liquid chromatography tandem mass spectrometry (LC-MS/MS) to examine the differential protein expression patterns between hypoxia and normoxia groups in the PDMS chip after 7 days of incubation. Proteomic experiments were outsourced to Acibadem Healthcare Group LABMED (Istanbul, Turkiye). Lyophilized samples were mechanically disrupted using magnetic beads (Retsch, Germany), and proteins were extracted with the Universal Protein Extraction Kit (UPX; containing 4% SDS, 0.1 M DTT, and 0.1 M Tris, pH 7.6) supplemented with a protease inhibitor cocktail. Samples were incubated at 95°C for 5 min, cooled to room temperature, and stored at 4°C for 1 h. After centrifugation (15,000 g, 10 min), the supernatant was collected and stored at -80°C. For

View Article Online
DOI: 10.1039/D5BM01824B

proteomic sample preparation, 50 µg of protein was processed using the filter aided sample preparation (FASP). Firstly, proteins were loaded onto 30 kDa MWCO centrifugal filters (Microcon 30, Merck Millipore) and washed with 8 M urea in 0.1 M Tris-HCl buffer (pH 8.5). Alkylation was carried out with 400 mM iodoacetamide (IAA) in the dark for 20 min, followed by repeated washing with urea and 50 mM ammonium bicarbonate. Proteins were digested overnight at 37°C with MS-grade trypsin (enzyme-to-protein ratio 1:50 in 50 mM ammonium bicarbonate). Peptides were recovered by centrifugation, desalted, and subjected to LC-MS/MS analysis. Peptide separation (400 ng) was performed by nanoLC, and analysis was carried out using a high-resolution mass spectrometer (Xevo G2-XS QTof, Waters, USA). Raw MS/MS spectra were searched against the UniProt protein database using Progenesis software. Label free quantification (LFQ) was applied, and significantly differentially expressed proteins were further analyzed for functional annotation and pathway enrichment using Metascape and STRING databases (22). Protein intensity values were log2 transformed and row Z-scores were calculated. Unsupervised hierarchical clustering was performed using the complete linkage method prior to heatmap generation. Differentially expressed proteins were identified using a threshold of $|\log2FC|>1$ and $-\log10(p\text{-value})>1.3$ and visualized as a volcano plot. Heatmap was generated using the pheatmap package (23) and volcano plots were created using ggplot2 (24) in R (25).

2.14. Determination of the astrocytic differentiation of the cells using anti-GFAP staining

In order to determine the differentiation properties of U87 cells with mono- and co-culture with microglia within the hydrogel, and under normoxic and hypoxic conditions in the chip model, immunofluorescence staining was conducted for GFAP. After 7 days of incubation within the PDMS chip (with or without the glass diffusion barrier), cells were washed with PBS (3 times, 5 min each), fixed with paraformaldehyde (4%, w/v) for 15 min, washed with PBS (3 times, 5 min each), and incubated in glycerol (100 mM in PBS) for 15 min. Following washes with PBS, cell membranes were permeabilized with Triton X-100 (0.1%, v/v, in PBST) for 10 min. Nonspecific binding was blocked with normal goat serum (5%, v/v, in PBST) for 1 h. Cells were then washed with goat serum (1%, v/v, in PBST) and incubated overnight at 4°C with the primary antibody (chicken anti-human GFAP IgY, 1:3000, v/v in 1% goat serum). After washing with 1% goat serum (3 times, 5 min each), cells were incubated with the secondary antibody (Alexa Fluor 488-conjugated anti-chicken IgY, 1:500, v/v in 1% goat serum) at 37°C for 1 h. Nuclei were counterstained with DAPI (1:5000 in PBS) for 10 min, washed with PBS

View Article Online
DOI: 10.1039/D5BM01824B

(3 times, 5 min each), and the samples were examined with CLSM (Zeiss LSM 900, Germany). The images were acquired using same gain and laser power settings. Fluorescence intensity analysis was performed using ImageJ (version 1.53k, NIH). GFAP and DAPI channel images were exported separately and converted to 8-bit grayscale. Cell nuclei were counted from DAPI channel images after manual thresholding, using the “Analyze Particle” function. GFAP fluorescence intensity was quantified by measuring the Raw Integrated Density of the entire image field. Background fluorescence was corrected by subtracting the mean intensity of a non-fluorescent region multiplied by the corresponding measurement area. The resulting values were normalized to cell count to obtain fluorescence intensity per cell.Brightness and contrast adjustments were applied equally across all images for visualization.

2.15. Invasion assay under normoxic and hypoxic conditions

For the assessment of invasion, spheroids composed of U87-EGFP and HMC3 cells were formed. Firstly, U87-EGFP (3.5x10^3 cells/100 µL) and HMC3 (1.5x10^3 cells/100 µL) cells were seeded into the wells of an ultralow attachment plates and incubated in an incubator (37°C, 5% CO_2). After 72 h incubation, compact spheroids formed. Cell free HAMA/dECM solution (1%, w/v HAMA and 3% w/v dECM, 1H3D) was prepared and printed into a disc structure (9 mm diameter, 1 mm height) using the printing parameters described in Section 2.5. Then, the compact spheroids were transferred into the center of the printed structures by gently pipetting, and crosslinked under UV (365 nm, 2 min). The constructs were then placed to the center of the PDMS chips with a glass diffusion barrier (hypoxia) or without a barrier (normoxia) and incubated for 5 days. Only U87 cells were EGFP-labeled in the co-culture system to specifically monitor GBM invasion. Spheroids were imaged daily using CLSM (Zeiss LSM 900, Germany). Spheroid radius was measured on Day 0 using ImageJ (version 1.53k, NIH). The image scale was set based on the scale bar present in the images prior to measurement. Invasion distance was calculated by measuring the distance from the spheroid center to the invading cell front for each point around spheroids. The initial spheroid radius was subtracted from each measurement to determine the net invasion distance.

2.16. Visualization of nutrient and drug flow

Transport of nutrient and drug within the printed constructs in the PDMS chip was modeled by diffusion using fluorescein (5 µM) in culture medium. The fluorescein containing medium was introduced into the chip via the medium channels, and its distribution was monitored for 24 h (at 0, 1, 2, and 24th h) using CLSM (Zeiss LSM 900, Germany) (17).

View Article Online
DOI: 10.1039/D5BM01824B

2.17. Testing of the platform with a model drug: temozolomide (TMZ)

Drug response in the GBM model was examined by determining the IC_{50} value of temozolomide (TMZ). TMZ stock solution (200 mM) was prepared in DMSO, and diluted to the desired concentrations in complete medium. In order to determine the concentration range, a preliminary Live/Dead assay was performed on cells treated with TMZ (0, 1000, 2500, and 5000 µM) for 72 h under hypoxic conditions. For cytotoxicity assessment, the cell-loaded hydrogels were cultured in the chips under hypoxic or normoxic conditions for 7 days. As a control, co-culture cells were grown on 2D monolayers for 24 h (to reach 80% confluency). Then, the medium was replaced with medium containing TMZ concentrations (0, 10, 100, 500, 1000, 1500, 2000, 2500 µM). Following 72 h incubation in a humidified incubator (37°C, 5% CO_2), cell viability was measured using the Alamar Blue assay. Firstly, the cell-loaded hydrogels in the chips were transferred to black well plates, alamar Blue reagent (10%, v/v in complete medium) was added to the wells, and incubated for 3 h at 37°C in a humidified incubator. Then, fluorescence was measured at ex/em: 560/590 nm using a microplate reader (Victor Nivo, PerkinElmer, USA). The viabilities were normalized to untreated controls. IC_{50} values were determined in GraphPad Prism (version 5.02) by nonlinear regression using a three parameter dose-response model (log[inhibitor] vs. normalized response, Hill slope=-1), and reported as best fit values with 95% confidence intervals.

2.18. Statistical analysis

Statistical differences between groups were determined using one-way ANOVA with Tukey post hoc test. For datasets with two independent variables, two-way analysis of variance (ANOVA) with a Bonferroni post hoc test was applied. Data were expressed as mean ± standard deviation (SD), and differences were considered statistically significant at $p<0.05$. Differences in IC_{50} values between groups were assessed using the extra sum-of-squares F-test. Analyses were performed using GraphPad Prism (version 5.02). For proteomics data, differential protein expression was determined using an unpaired two tailed Student's t-test with Benjamini-Hochberg false discovery rate (FDR) correction (FDR<0.05). Proteins with a fold change≥1.2 and adjusted $p<0.05$ were considered significantly differentially expressed.

3. Results

3.1. Modeling hypoxia within the bioprinted glioblastoma-microglia structure

In order to develop a GBM model, the suitability of the HAMA/dECM composites for extrusion printing was examined firstly. Printability and rheological characterization were performed to

View Article Online
DOI: 10.1039/D5BM01824B

identify a formulation capable of maintaining structural fidelity during printing while supporting cell viability. Different HAMA/dECM hydrogel formulations were examined for their rheological and printing performance. In extrusion bioprinting, shear thinning facilitates smooth and continuous extrusion with minimal cell damage, while thixotropy and yield stress ensure post printing structural stability, and together these rheological features determine the overall printability of bioinks (26, 27). All tested formulations, containing 1% (w/v) HAMA and 1-3% (w/v) dECM, exhibited shear thinning behavior, decreasing of viscosity as shear rate increased, which prevents nozzle clogging and ensures continuous and uniform filament formation. Thixotropic analysis demonstrated rapid recovery of viscosity after high shear stress, indicating post printing recovery. Printability tests with different internal patterns (rectangular and hexagonal) revealed that lower viscosity formulations with lower dECM content (1-2% w/v) lacked stability for consistent extrusion, while the optimized composition (1%, w/v HAMA and 3% w/v dECM) leads to continuous filament deposition and retention of shape after printing. Using the optimized formulation and printing parameters, the GBM construct was fabricated with U87 cells as the four layer thick inner core, surrounded by a four-layer ring of HMC3 cells (Fig. 1). This design aimed to mimic the spatial organization of tumor-microglia to study the interactions within the glioblastoma microenvironment. Characterization with SEM (Fig. 3A) revealed that the cell free matrix exhibited an interconnected porous architecture, with an average pore size of 270 ± 21 μm, which is suitable for cell infiltration and nutrient transfer. The cell loaded hydrogel (Fig. 3B) displayed networks of cellular extensions spanning across the pores and the presence of ECM-like fibrillar structures, suggesting active cell adhesion and potential matrix remodeling during culture. Cell viability in the printed co-culture constructs remained above 90% (Fig.3C-F), confirming that the printing process effectively supported cell survival over 14 days. High viability was similarly maintained in U87 and HMC3 monocultures (Fig. 3G), as well as across HAMA-only, dECM-only, and HAMA/dECM formulations, confirming the biocompatibility of the hydrogel composition and its individual components.

View Article Online
DOI: 10.1039/D5BM01824B

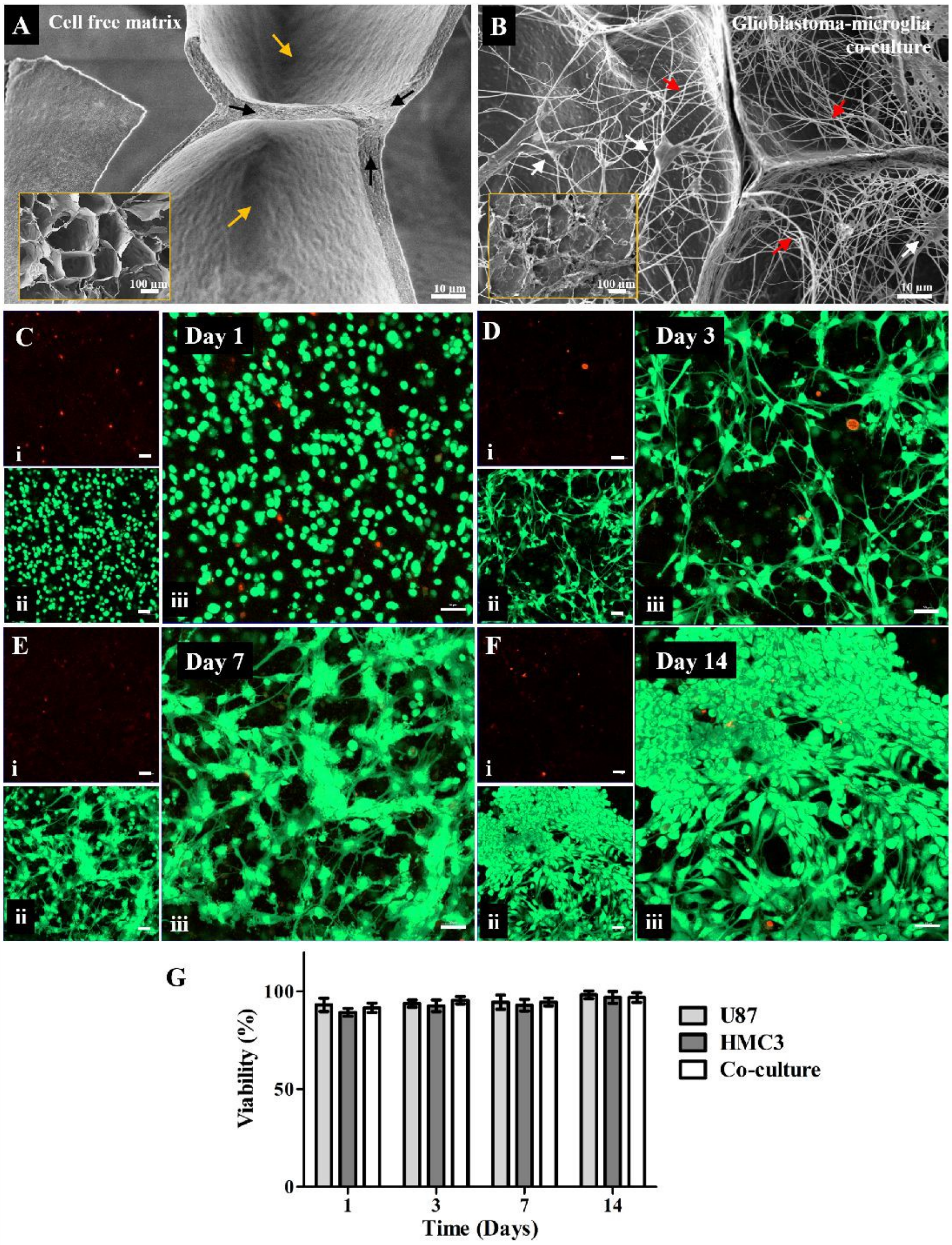

Figure 3. The bioprinted glioblastoma-microglia co-culture. SEM images of (A) the cell free matrix, and (B) the same matrix after co-culture with glioblastoma-microglia cells. Black arrows indicate crosslinked networks, yellow arrows show the interconnected pores. White arrows indicate the cells, red arrows show ECM-like fibrillar structures. Scale bar: (A, B) 10 µm, insert: 100 µm. (n=3 samples per group). (C-F) Live/Dead analysis of the bioprinted U87/HMC3 co-culture on days (C) 1, (D) 3, (E) 7, and (F) 14. (i) The dead cells (stained with ethidium homodimer-1, red), (ii) the viable cells (stained with calcein AM, green) and (iii) merged. Scale bar: 50 µm. (G) Viability of U87, HMC3, and co-culture cells within the hydrogel system at days 1, 3, 7, and 14, quantified from Live/Dead images. Data is presented as mean ± SD (n=3 samples per group).

View Article Online
DOI: 10.1039/D5BM01824B

The PDMS platform was designed to create an oxygen gradient from the periphery toward the center, with decreasing oxygen toward the core (Fig 4A). Consistent with this design, constructs cultured with the glass barrier exhibited intense green fluorescence in the central regions, indicating pronounced hypoxia, while peripheral regions displayed markedly lower fluorescence (Fig. 4D). The hydrogel construct itself may also limit oxygen diffusion, resulting in a relatively hypoxic microenvironment (28). When cells loaded in the hydrogels were cultured without the glass barrier, a moderate green fluorescence signal was detected, yet its intensity was markedly lower (Fig. 4C), similar to that observed at the periphery of the hypoxia chip. These results demonstrate that the glass barrier served its purpose and prevented atmospheric O_2 diffusion, thus creating a graded hypoxic environment that increased from the periphery to the center (Fig. 4B).

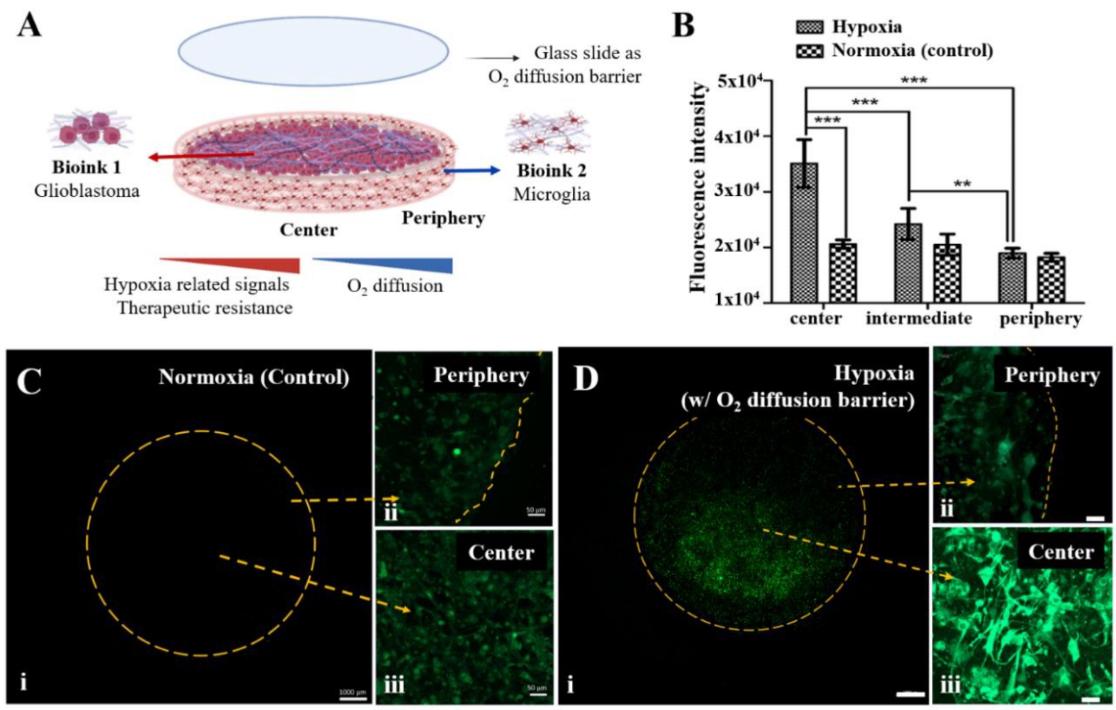

Figure 4. Hypoxia in the PDMS chip. (A) The hypoxia chip components. (B) Quantification of mean fluorescence intensity in the center, intermediate, and periphery regions under hypoxic and normoxic conditions. CLSM images of the cells in the PDMS chip (C) without glass barrier (normoxia) and (D) with glass barrier (hypoxia): (i) whole chip view, (ii) periphery, and (iii) center. Green: hypoxic cells stained with Image-iT Green Hypoxia Reagent. Orange dashed lines indicate hydrogel borders. Scale bars: (i) 1000 μm; (ii, iii) 50 μm. Data is presented as mean ± SD (n=6 samples per group from 3 independent experiments), and statistical comparisons were performed using two-way ANOVA followed by Bonferroni post-hoc test. ***p < 0.001, p** < 0.01.

View Article Online
DOI: 10.1039/D5BM01824B

3.2. Hypoxia produces histopathologic features of GBM

Viability and proliferation patterns of U87/HMC3 co-cultures in the hypoxia chip were determined using a Live/Dead assay (Fig. 5) and Ki-67 immunofluorescence staining (Fig. 6). The central region of the hypoxia chip exhibited a distinct necrotic core composed predominantly of dead cells, resembling the necrosis characteristic of GBM tumors arising from oxygen and nutrient deprivation. As expected, the intermediate and peripheral regions contained mostly viable cells, suggesting reduced hypoxia and improved nutrient availability in these areas. Immunofluorescence staining with the proliferation marker Ki-67 further confirmed this pattern (Fig. 6A,B). The results showed that Ki-67 expression was significantly lower and nearly absent in the cells in the center of the chip compared to those in the intermediate and peripheral regions, indicating increased proliferative activity toward the periphery. This spatial distribution resembles the pathological feature of GBM, in which proliferating tumor cells form concentric layers surrounding a necrotic core.

View Article Online
DOI: 10.1039/D5BM01824B

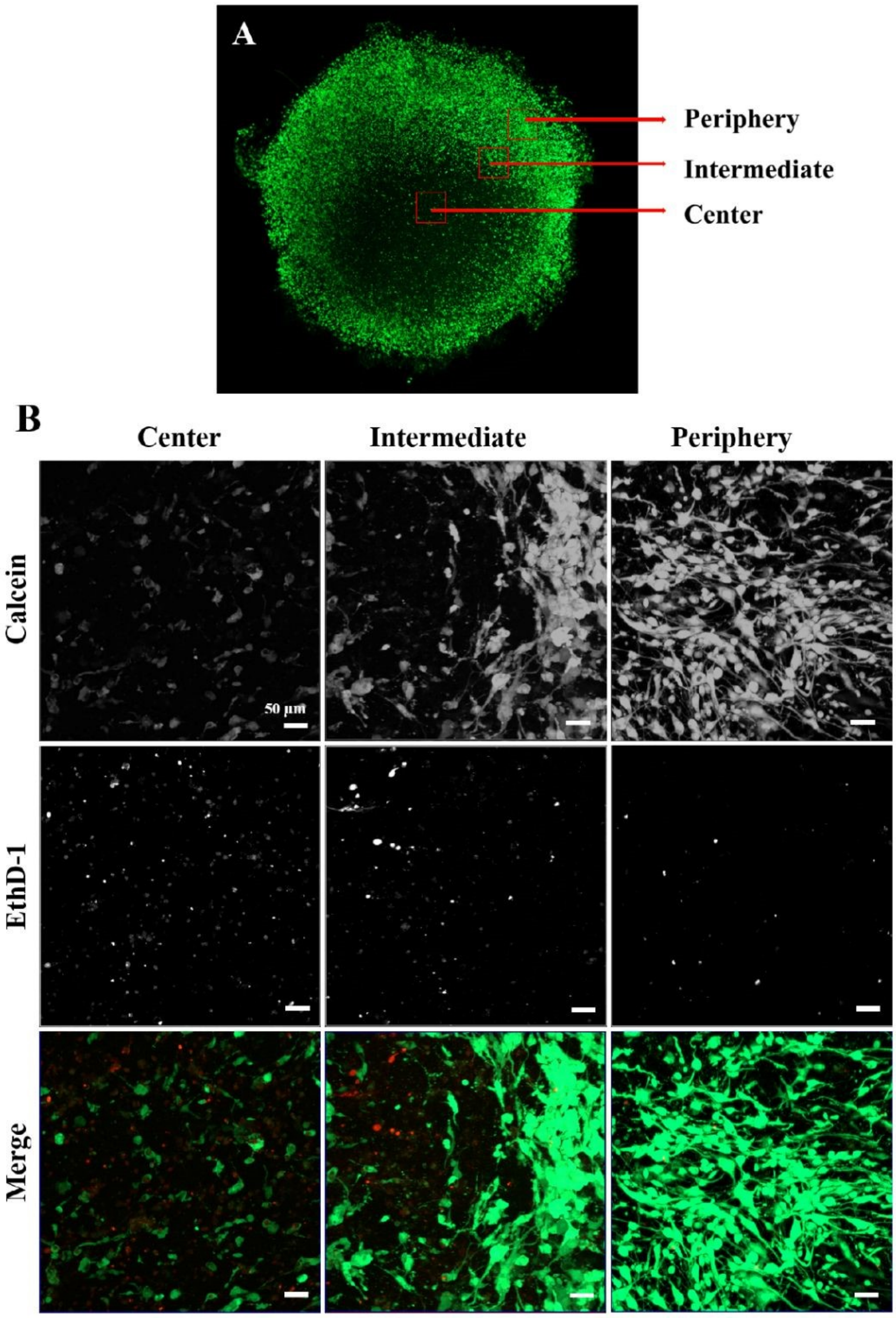

Figure 5. Regional analysis of viability in the hypoxia chip. (A) Whole chip fluorescence image indicating the center, intermediate, and periphery regions. (B) Live/dead staining in the center, intermediate, and periphery regions. Green: viable cells (Calcein AM), red: dead cells (ethidium homodimer-1). Scale bars: 50 µm. (n=3 samples per group)

View Article Online
DOI: 10.1039/D5BM01824B

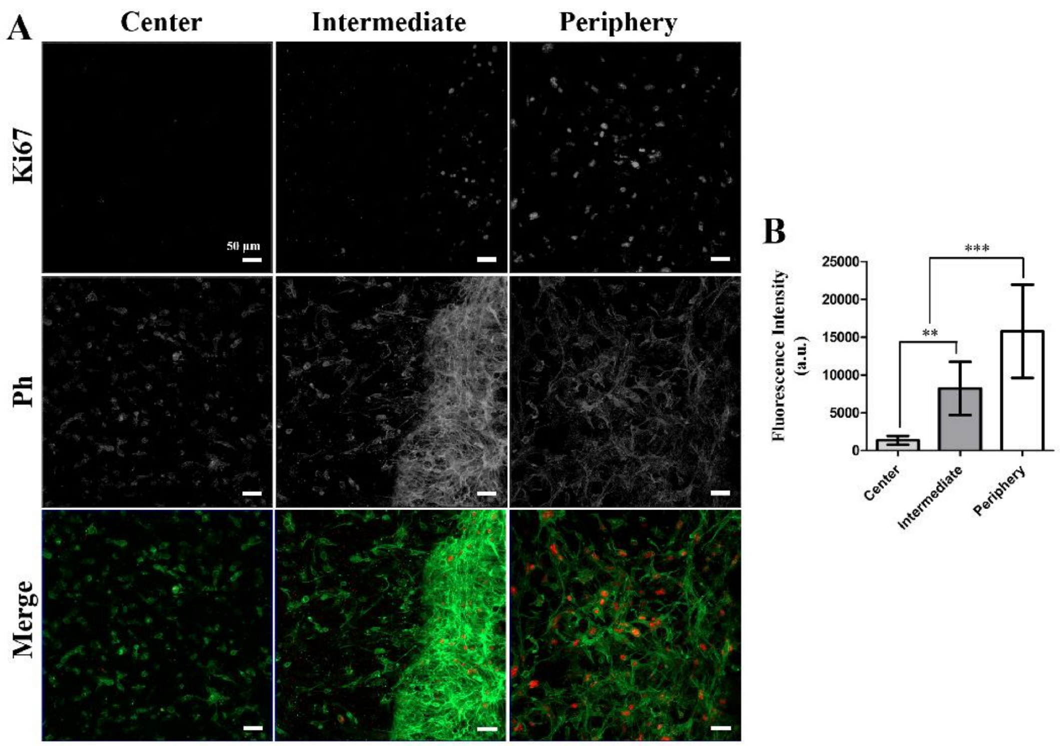

Figure 6. Regional analysis of proliferation in the hypoxia chip. (A) Ki-67/Phalloidin staining in the center, intermediate, and periphery regions. Green: F-actin (phalloidin), red: Ki-67 positive proliferating cells. Scale bars: 50 µm. (B) Quantification of Ki67 fluorescence intensity in the center, intermediate, and periphery regions. Data is presented as mean ± SD (n=3 samples per group), and statistical comparisons were performed using one-way ANOVA followed by Tukey's post-hoc test. ***$p < 0.001$, p** < 0.01.

3.3. Hypoxia induces transcriptional and proteomics changes

Gene expression analysis was performed to examine the effects of hydrogel platform and hypoxia on cellular adaptation and their resemblance to *in vivo* tumors (Fig. 7A). The results indicated that under normoxic conditions, Ki67 and EGFR, key regulators of cell growth and survival, showed significantly higher expression in hydrogel compared to monolayer cultures, with further upregulation observed under hypoxia (Fig. 7B). Similarly, CHI3L1 expression was elevated in hydrogels under normoxia, and further increased under hypoxia. In contrast, stemness and therapy resistance associated genes (HIF1α, SOX2, and NES) exhibited minimal change in normoxia but were significantly upregulated under hypoxic conditions. In contrast, GFAP expression did not change significantly in both normoxic and hypoxic 3D cultures compared to monolayer controls.

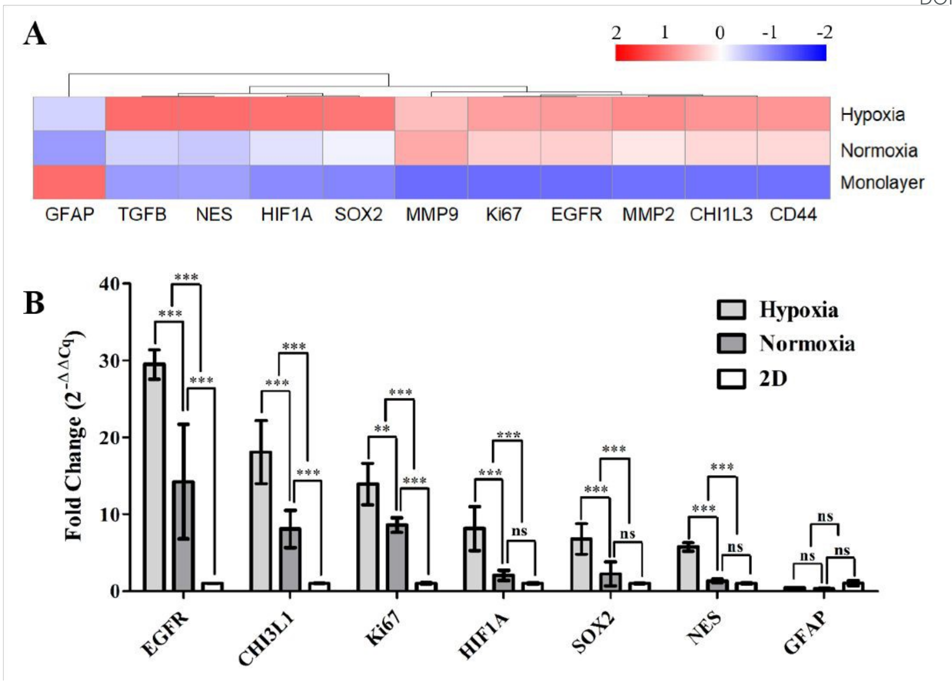

Figure 7. Gene expression analysis of the cells cultured in PDMS chips under normoxic and hypoxic conditions. (A) Heatmap showing relative gene expression across hypoxia, normoxia, and monolayer conditions. Z-score normalized fold change values across experimental groups were visualized with color scale ranges from -2 (blue) to 2 (red), with white indicating a Z-score of 0. Quantification of growth, proliferation, and tumor development related genes (EGFR, CHI3L1, and Ki67) and hypoxia, stemness, and therapy resistance related genes (HIF1α, SOX2, NES, and GFAP). Data is presented as fold change ($2^{-\Delta\Delta Cq}$) relative to 2D monolayer cultures. (n=8 samples per group from 3 independent experiments). Statistical comparisons were performed using two-way ANOVA with a Bonferroni post-hoc test. ***$p < 0.001$, $p^{**} < 0.01$, ns: not significant.

Immunofluorescence staining was performed for GFAP to assess the differentiation of cells into astrocytes under normoxic and hypoxic conditions (Fig. 8). In U87/HMC3 co-cultures, GFAP expression was 47.7% lower compared to U87 monocultures in the hydrogel under normoxic conditions, indicating that the presence of microglia reduces astrocytic differentiation in glioblastoma cells. This reduction was even greater under hypoxic conditions, where GFAP expression levels decreased by 30.9% compared to normoxic co-cultures. In the hypoxia group, cells appeared smaller with altered morphology compared to normoxic conditions. These findings suggest that microglia and hypoxia together promote a shift from astrocytic differentiation toward a mesenchymal-like phenotype, a characteristic feature of high grade gliomas (29).

View Article Online
DOI: 10.1039/D5BM01824B

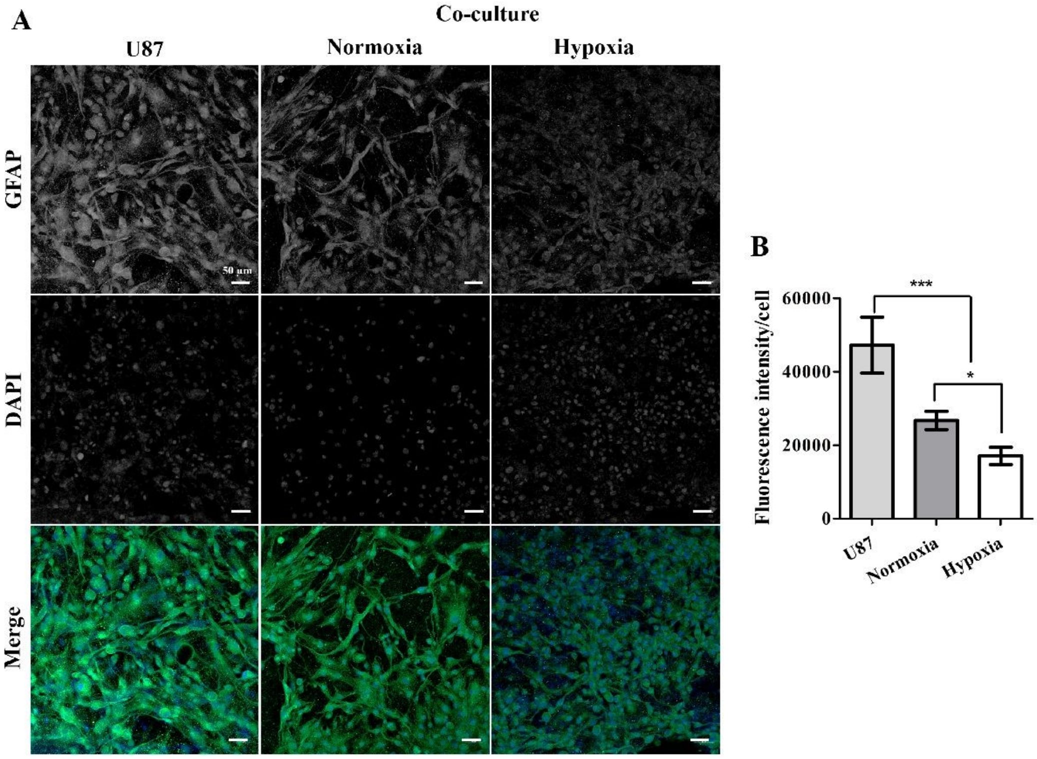

Figure 8. Immunofluorescence staining against GFAP. (A) CLSM images of the cells under normoxic and hypoxic conditions. Scale: 50 µm. (B) Graph shows relative fluorescence intensity (GFAP-Alexa Fluor 488) per cell. Data is presented as mean ± SD (n=3 samples per group), and statistical comparisons were performed using one-way ANOVA followed by Tukey's post-hoc test. $^{***}p < 0.001$, $^{*}p < 0.05$.

In order to investigate the pathways involved in hypoxia induced adaptations in the model, label free quantitative proteomic profiling was performed comparing hypoxic and normoxic conditions. Heatmap clustering (Fig. 9A) showed clear separation between normoxia and hypoxia samples, indicating consistent proteomic shifts in response to hypoxia. Volcano plot analysis revealed 16 upregulated and 10 downregulated proteins in hypoxic compared to normoxic conditions (Fig. 9B). Kyoto Encyclopedia of Genes and Genomes (KEGG) pathway enrichment analysis of the significantly upregulated proteins under hypoxic conditions indicated activation of glycolysis/gluconeogenesis, carbon metabolism, amino acid biosynthesis, mineral absorption, and HIF1 signaling (Fig. 9D). Protein-protein interaction (PPI) network analysis (Fig. 9C) revealed a highly connected glycolysis module, including lactate dehydrogenase (LDHAL6B), triosephosphate Isomerase (TPI1), pyruvate kinase (PKLR), phosphoglycerate kinase (PGK1), glucose-6-phosphate isomerase (GPI), and enolase 1 (ENO1), which regulate metabolic reprogramming in GBM, supporting anaerobic glycolysis and potentially contributing to adaptation in oxygen deprived tumor regions (30-32).

View Article Online
DOI: 10.1039/D5BM01824B

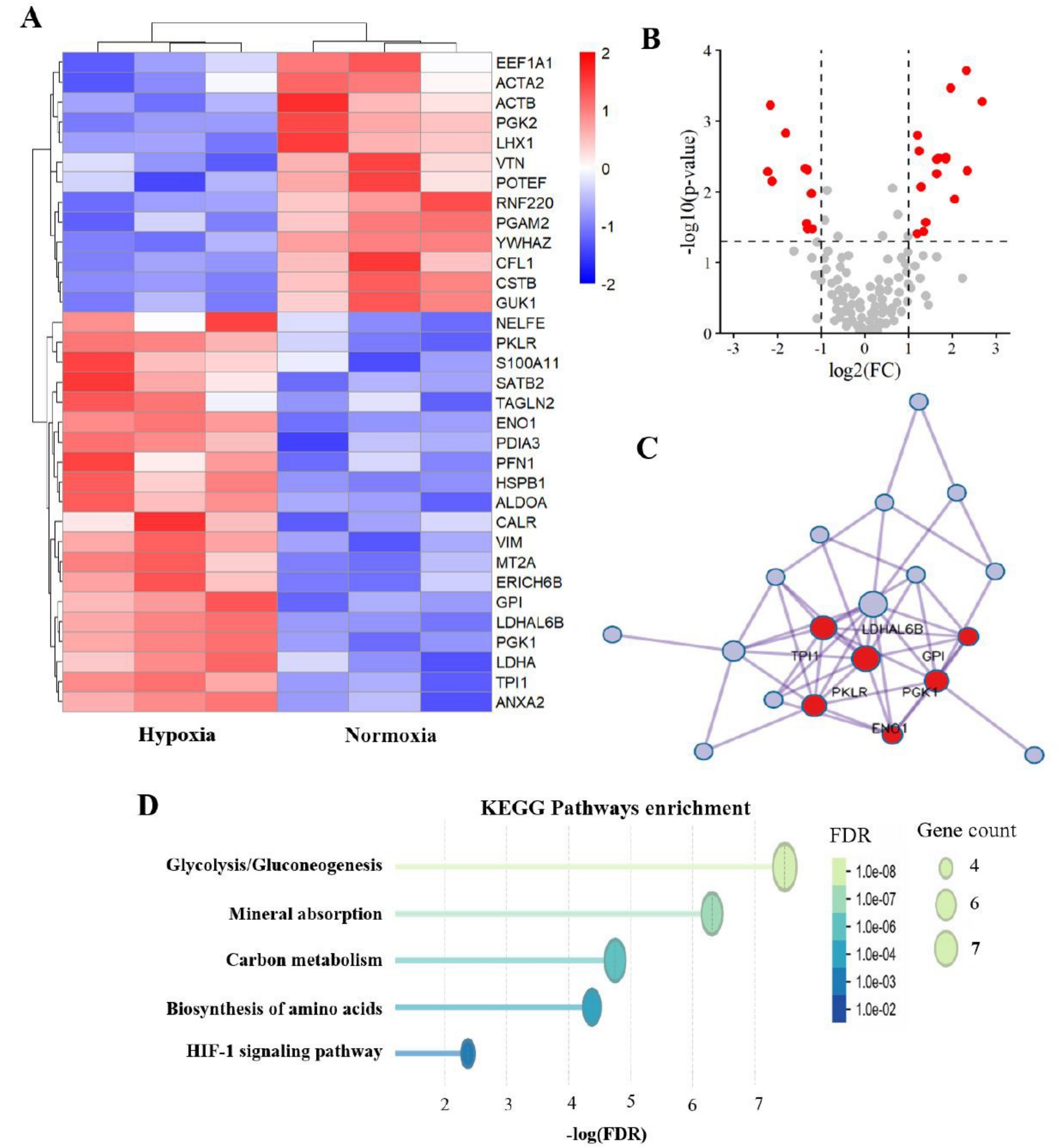

Figure 9. Proteomic analysis of hypoxia chip model. (A) Heatmap showing relative abundance patterns of significantly altered proteins ($p < 0.05$). Row Z-score normalized protein expression values across experimental groups were visualized with color scale ranging from -2 (blue) to 2 (red), with white indicating a Z-score of 0 (n=3 samples per group). (B) Volcano plot showing the identified proteins. Differentially expressed proteins ($|\log2FC| > 1$, $-\log10(\text{p-value}) > 1.3$) were highlighted in red, remaining proteins are in grey. (C) PPI network of significantly upregulated proteins generated in Metascape, highlighting a core glycolysis pathway cluster in red. (C) KEGG pathway enrichment of upregulated proteins performed in STRING.

3.4. Hypoxia enhances invasive behavior of GBM

In order to assess the invasive potential of GBM cells under hypoxic conditions, an invasion assay was performed using spheroids composed of U87-EGFP and HMC3 cells. EGFP labeling enabled separate tracking of GBM cells within the co-culture system. Spheroids were preferred

View Article Online
DOI: 10.1039/D5BM01824B

over bioprinted cell constructs as they provided a more compact and well defined initial geometry, enabling clearer and more reproducible comparisons between experimental groups. The boundaries of bioprinted cell structures were less sharply defined, which could introduce variability in invasion distance measurements. The assay revealed clear differences in glioblastoma cell invasion between normoxic and hypoxic conditions (Fig. 10), with invasion increasing over time in both groups (Fig. 10A, B). In the early stages, spheroids remained compact, showing minimal outward migration. However, spheroids under hypoxia exhibited early signs of migration, with cellular extensions penetrating the surrounding matrix. Over time, spheroids under hypoxia exhibited significantly greater cell migration and expansion (32%) than spheroids under normoxia. These findings were supported by molecular analysis, which showed increased expression of invasion related genes. Under both normoxic and hypoxic conditions within the hydrogel platform, MMP2, MMP9, TGF-β and CD44 genes were significantly upregulated compared to monolayer cultures. MMP2, TGF-β and CD44 levels were also significantly higher under hypoxia than in normoxic 3D conditions (Fig. 10C). Together, these data suggest that hypoxia promotes GBM invasion, likely through enhanced extracellular matrix degradation and cell migration.

View Article Online
DOI: 10.1039/D5BM01824B

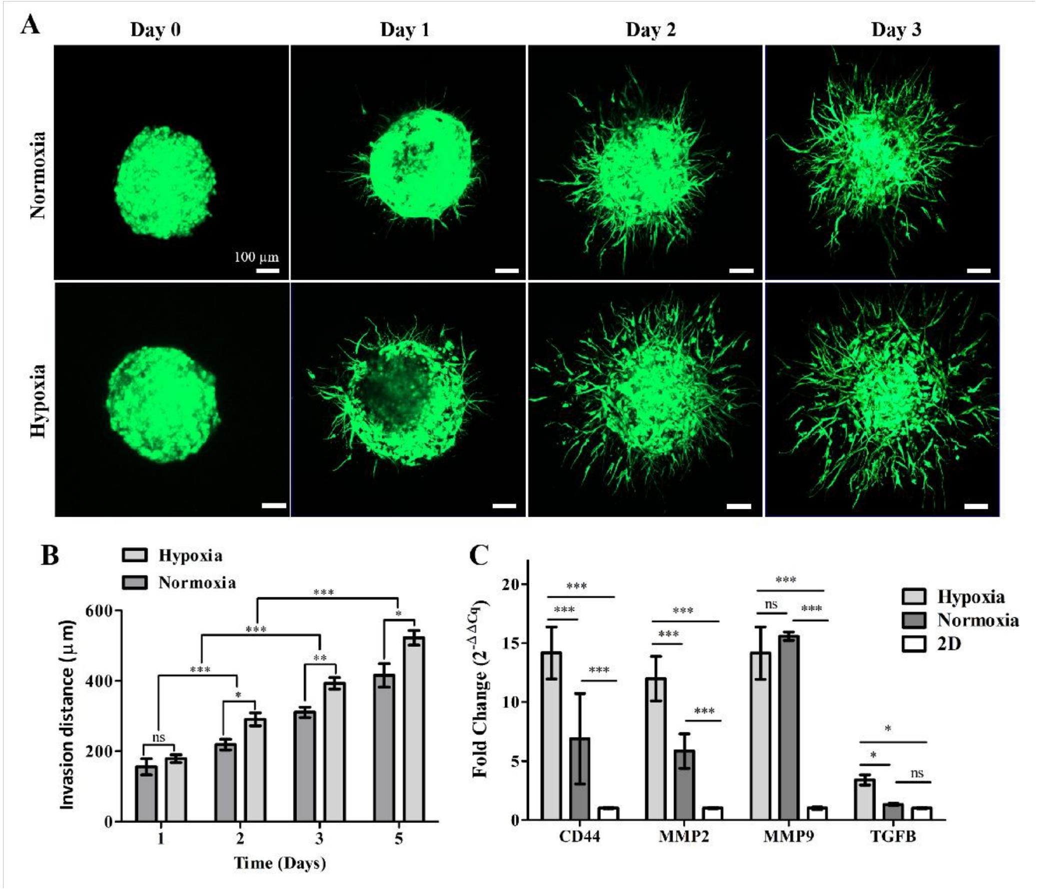

Figure 10. Glioblastoma invasion in the PDMS chip. (A) CLSM images of the glioblastoma cell invasion. Green: EGFP labeled U87 cells. Scale: 100 μm. (B) Invasion distances were measured for 5 days. Data is presented as mean ± SD (n=3 samples per group), and statistical comparisons were performed using two-way ANOVA followed by Bonferroni post-hoc test. ***$p < 0.001$, p** < 0.01. (C) Quantification of invasion related gene expressions (MMP2, MMP9, CD44, TGF-β). Data is presented as fold change ($2^{-\Delta\Delta Cq}$) relative to 2D monolayer culture (n=8 samples per group from 3 independent experiments). Statistical comparisons were performed using two-way ANOVA with a Bonferroni post-hoc test. ***$p < 0.001$, p** < 0.01, *$p < 0.05$, ns: not significant.

3.5. Hypoxia promotes chemoresistance to temozolomide

Diffusion of fluorescein (molecular weight of 0.4 kDa) within the hydrogel was monitored for 24 h to simulate the transport behavior of low molecular weight drugs such as TMZ (Fig. 11A). Fluorescence imaging analysis revealed a clear time dependent diffusion profile. Initially (0 h), no fluorescence signal was detected within the hydrogel. By 1 h, a fluorescence signal was observed progressing from the periphery toward the center, indicating inward diffusion from the hydrogel edges. At 24 h, fluorescence intensity was uniformly distributed, suggesting that diffusion had reached equilibrium.

In order to test the model, the cytotoxic response of the cells to TMZ was assessed. Live/Dead assay showed that 2500 μM TMZ induced pronounced cell death (Fig. 11B), therefore, 0-2500

View Article Online
DOI: 10.1039/D5BM01824B

μM was selected as the concentration range for subsequent cytotoxicity experiments. Following 72 h treatment with TMZ, cell viability was subsequently quantified, and IC_{50} values were derived from the corresponding dose-response curves (Fig. 11C). In 2D monolayer cultures, IC_{50} was calculated to be 320 μM (95% CI: 153.4-668.4), whereas in the chip model, IC_{50} values were 698 μM (95% CI: 489.7-911.3) under normoxia and 1091 μM (95% CI: 851.4-1399) under hypoxia (Fig. 11D). The higher IC_{50} values in the 3D model, particularly under hypoxic conditions, indicate increased chemoresistance to TMZ due to the physiological relevance of the model, which closely mimics *in vivo* oxygen gradients.

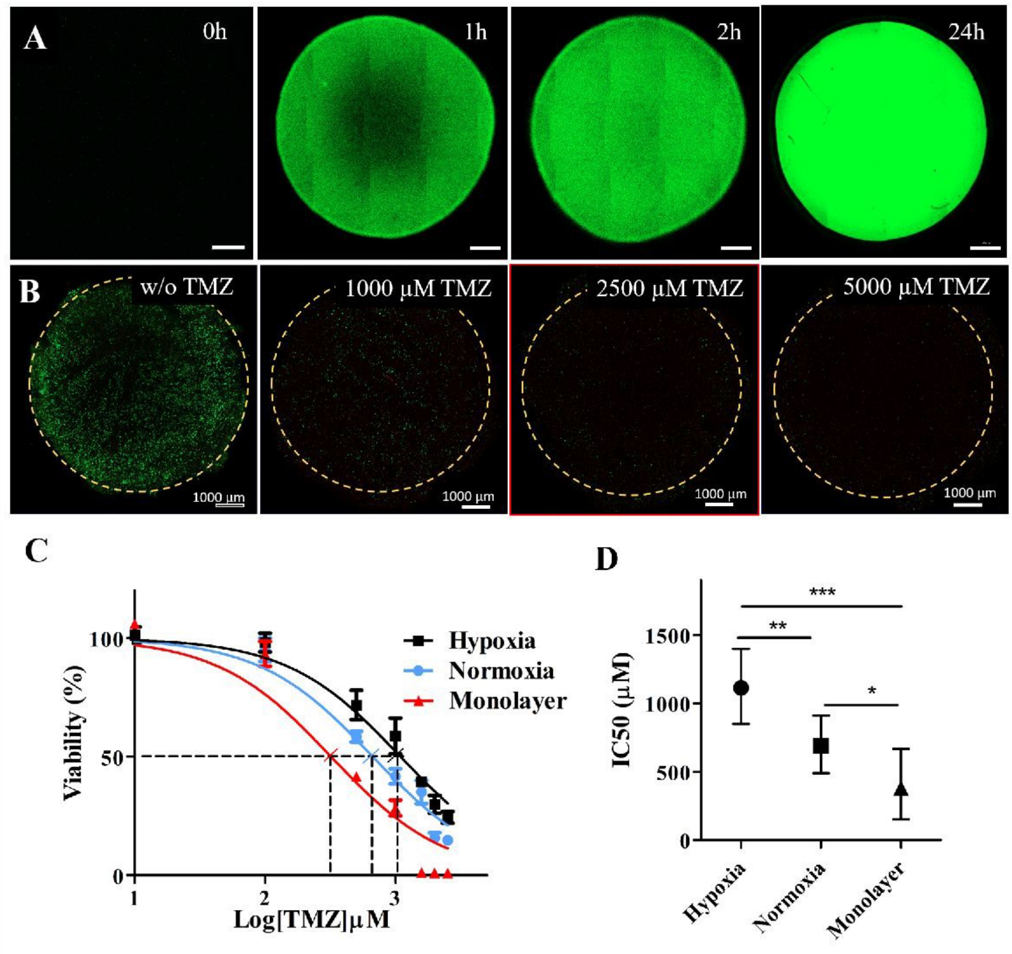

Figure 11. Visualization of molecular diffusion in the hydrogel and testing the chip model with TMZ. (A) Fluorescence images showing the diffusion of fluorescein (0 h, 1 h, 2 h, and 24 h) from the periphery toward the center of the hydrogel. Scale bars: 1000 μm. (n=3 samples). (B) Fluorescence images of co-cultures in the hypoxia chip treated with different TMZ concentrations for 72 h. Scale bars: 1000 μm. (n=2 samples). (C) Dose-response curves for TMZ in hypoxic, normoxic, and monolayer cultures. Data is presented as mean ± SD (n=6 samples per group from 2 independent experiments). The curves were fitted using a three-parameter dose-response model (log[TMZ] vs. normalized response, Hill slope=-1). (D) IC_{50} values for hypoxic, normoxic, and monolayer cultures with 95% confidence intervals derived from nonlinear regression. Statistical comparisons were made using the extra sum-of-squares F-test. $^{*}p < 0.05$, $^{**}p < 0.01$, $^{***}p < 0.001$.

View Article Online
DOI: 10.1039/D5BM01824B

4. Discussion

GBM tumors exhibit resistance to conventional therapies, shaped by a complex microenvironment comprising dense ECM, diverse cellular populations, and hypoxic gradients (33-35). Therefore, replicating these features *in vitro* is essential to better understand tumor biology and treatment response. In this study, a PDMS based hypoxia chip combined with a biomimetic hydrogel was developed to reproduce the pathological characteristics of GBM tumors. In our previous study, we formulated HAMA/dECM composite hydrogel which retained native ECM components and exhibited mechanical and rheological properties similar to those of GBM tissue, and supported key glioblastoma cell behaviors (19). The PDMS based hypoxia chip developed in this study further reproduced key characteristics of the glioblastoma microenvironment, offering a useful platform for investigating hypoxia related cellular behaviors. Using glass slide as a diffusion barrier enabled the formation of oxygen gradients, as indicated by Image-iT hypoxia staining, which showed higher fluorescence intensity in the hydrogel center compared to the periphery. This approach enabled the generation of hypoxic conditions without the need for complex instrumentation or chemical agents. Previous studies using diffusion barriers, such as PMMA layers (36) and PC films (11), have created hypoxic conditions, however, their closed system design limited the flexibility to include layered structures. In contrast, our model allows the integration of multicellular layers or organotypic cultures within a single platform, enabling more physiologically relevant *in vitro* models.

In order to examine the ability of the model to mimic GBM characteristics, key markers associated with proliferation, invasion, stemness, and therapy resistance were analyzed. HIF1α, SOX2, and NES, key regulators of stemness and therapeutic resistance, exhibited minimal expression in 3D cultures under normoxia but were significantly upregulated under hypoxia, suggesting that matrix cues alone do not activate stem-like programs and hypoxia is the primary trigger of stemness in our model (37-39). Macharia et al. (2021) demonstrated that exposure of GBM cells to 1% O_2 in 2D culture upregulated SOX2 expression, indicating that hypoxia can initiate reprogramming toward a stem-like state (40). Immunofluorescence analysis showed a significant decreases in GFAP levels under hypoxia and, suggesting that hypoxic conditions promote a less differentiated, stem-like, and potentially more aggressive tumor phenotype (29). Shah et al. (2021) similarly reported that glioblastoma cells cultured in 3D gelatin methacrylate hydrogels, unlike those in 2D, showed reduced GFAP and increased CD44 and MMP2 expression, reflecting mesenchymal reprogramming patterns seen *in vivo* (41). It was reported that hypoxia promotes mesenchymal transition in glioblastoma by activating transcription

View Article Online
DOI: 10.1039/D5BM01824B

factors such as HIF1α, especially in hypoxic and necrotic tumor areas (42). Consistent with this, our hypoxia model showed increased HIF1α, CD44, and MMP2 expression. Interestingly, the transcriptional profile also showed increased EGFR and Ki67 levels, suggesting a mixed phenotype combining proliferative and mesenchymal features. Supporting this, recent 3D spatial analyses of glioblastoma tumors showed that mesenchymal and proliferative traits are often observed together within the same tumor (43). Rather than leading to a complete lineage transition, hypoxia facilitates a mesenchymal-proliferative state, indicating heterogeneity of glioblastoma cells under low oxygen conditions.

Proteomic profiling further confirmed the relevance of the model, showing that hypoxic conditions triggered signaling pathways known to be associated with aggressive glioblastoma (44). Enrichment and network analysis showed that there were hypoxia related increases in glycolysis, carbon metabolism, amino acid biosynthesis, and HIF1 signaling pathways. These data is consistent with the phenotypic and transcriptional changes seen in this model. Notably, enrichment of the HIF1 signaling pathway suggests an activation of transcriptional programs that regulate metabolic and structural changes. Diffusion limitations within hydrogel systems, especially under hydpoxic conditions, can drive extracellular acidification and spatial metabolic heterogeneity by restricting local oxygen and nutrient availability and slowing transport of metabolic byproducts such as lactate and protons. Hypoxic tumor regions shift toward glycolytic metabolism and export lactate, while normoxic regions use it as a metabolic substrate, a reverse Warburg type effect that supports metabolic coupling across tumor cell populations (45, 46). Proteomic analysis revealed significant upregulation of glycolysis-associated pathway enzymes, including LDH, under hypoxic conditions. Since lactate accumulation and HIF-driven glycolytic signaling are closely linked to tumor aggressiveness, immune modulation, and therapy resistance in GBM (47), these parameters may offer predictive insight into cellular behavior within the hydrogel microenvironment. Direct pH and lactate measurements and metabolomic analyses are needed to further characterize the metabolic dynamics of this platform. Hypoxic conditions also drive metabolic coupling between GBM and microglia, simultaneously promoting immunosuppression and tumor progression. Lactate accumulation induces epigenetic reprogramming in microglia through histone lactylation, shifting them toward an immunosuppressive M2 phenotype. In turn, M2 microglia secrete immunomodulatory cytokines that can enhance glycolytic signaling in GBM cells, increasing lactate production (48). However, our previous proteomic comparison of GBM-microglia co-culture and GBM monoculture showed only limited enrichment of

View Article Online
DOI: 10.1039/D5BM01824B

glycolysis related processes, suggesting that hypoxia, rather than microglia-mediated metabolic reprogramming, may be the primary driver of the glycolytic shift observed in our model. Overall, these findings suggest that the hypoxia chip platform represents certain characteristics of metabolic and microenvironmental adaptation associated with glioblastoma. Nonetheless, different regions within a single tumor can display distinct molecular profiles. Therefore, it would be essential to perform advanced techniques such as spatial transcriptomics or single-cell RNA sequencing for gaining detailed insight on tumor heterogeneity and region specific expression and adaptability driven by hypoxic conditions in the model.

Glioblastoma cells under hypoxia demonstrated significantly greater invasion than those under normoxic conditions. Supporting this finding, MMP2, CD44, and TGF-β expressions were also upregulated, suggesting that hypoxia enhances invasiveness through ECM remodeling, cell-matrix interactions, and activation of epithelial-to-mesenchymal transition (EMT) and cytoskeletal reorganization (49, 50). The correlation between these transcriptional alterations and the observed invasion patterns demonstrates the role of hypoxia driven signaling mechanisms in glioblastoma aggressiveness. These findings are consistent with previous reports showing that hypoxia induced HIF1α activation alters gene expression profile, promoting a mesenchymal-like transition that increases glioblastoma cell motility, invasion, and resistance to therapy (51). Although the increased invasion observed was largely due to hypoxia induced pathways, other factors such as ECM and microglia signaling should also be considered. In our previous study using the same HAMA/dECM matrix, we showed that microglia co-culture increased glioblastoma invasion even under normoxia, indicating their intrinsic protumoral role (19). Therefore, the further increase in invasion associated markers and invasion distance under hypoxia suggests that low oxygen conditions act synergistically with microenvironmental cues, rather than function independently. ECM also acts as a dynamic regulator of tumor progression and therapeutic response. Since cell-ECM interactions, including HA-CD44 ligand signaling and mechanotransduction, depend on intrinsic cell properties (52), patient-derived cells may respond differently to the same ECM-derived cues and induce distinct remodeling patterns. Integrating patient derived cells into this ECM mimetic hydrogel alongside molecular imaging modalities such as PET, MRI, and SPECT could enable dynamic spatial characterization of ECM remodeling and provide predictive insight into patient-specific therapeutic responses (53). The tunable nature of the platform further allows modulation of matrix composition and mechanical properties, supporting the modeling of patient-specific tumor microenvironments that reflect interpatient variability.

View Article Online
DOI: 10.1039/D5BM01824B

In GBM tumors, pseudopalisading necrosis pattern is largely driven by hypoxia induced signaling and nutrient gradients, which promote proliferation and migration toward regions with greater oxygen and nutrient supply (6). The hypoxia chip reproduced this spatial heterogeneity by generating a necrotic core surrounded by proliferative tumor regions. Ki-67 expression and viability patterns within the model indicated the pseudopalisading necrosis characteristic of GBM.

The *in vitro* model system was also examined for its response to TMZ under normoxic and hypoxic conditions. While DMSO controls were not included in TMZ treatment experiments due to throughput and sample number limitations of the platform, a separate cytotoxicity assessment in co-cultured GBM-microglia monolayers confirmed that DMSO concentrations within the treatment range (up to 1.25%) did not induce significant cytotoxicity. The IC_{50} value for TMZ was found to be significantly lower in monolayer cultures compared to hydrogel cultures under normoxia, while hypoxic conditions further increased the IC_{50} value by 56%, indicating increased chemoresistance. These findings are consistent with previous reports signifying reduced drug penetration within 3D matrices due to high ECM density, which acts as a diffusion barrier and limits drug access to cells (54). In addition, hypoxic microenvironments are known to promote drug resistance within glioma cells due to its effects on modulation of gene expression, quiescence inducing effects, and survival signaling, which are contributing to the higher IC_{50} values under hypoxic conditions (55). However, the impact of hypoxia on glioblastoma behavior is highly dependent on the microenvironment. Musah-Eroje and Watson (2019) showed that while hypoxia had minimal effects on temozolomide resistance in 2D cultures, the same cells showed significantly increased resistance in a 3D model, particularly under low oxygen conditions. This suggests that hypoxia alone is insufficient to drive therapeutic resistance without combined with ECM signals and spatial gradients (56). Therefore, the increased resistance and metabolic changes observed in our model likely result from the combined effects of hypoxia and the 3D microenvironment. Microglia has also been shown to contribute to TMZ resistance in glioblastoma (57). However, a hypoxic GBM monoculture condition was not included in the study, limiting the ability to distinguish microglia-specific effects from hypoxia-driven responses. Despite this, our previous findings showed that GBM-microglia co-culture within the hydrogel promoted proliferation, and upregulation of MMP2, MMP9, and TGF-β relative to both GBM monoculture within the hydrogel and monolayer cultures under normoxic conditions. Given that pro-tumorigenic microglias are known to secrete MMPs and TGF-β (58), these results suggest that hydrogel

View Article Online
DOI: 10.1039/D5BM01824B

derived signals and GBM-microglia interactions contribute to a pro-tumoral microenvironment. Previous proteomic comparison of GBM-microglia co-culture and GBM monoculture under normoxic conditions identified enrichment of biological processes relevant to therapeutic response, including cellular oxidant detoxification (19). Since TMZ induces ROS-mediated tumor cell death, enhanced antioxidant and ROS-detoxification capacity may reduce treatment induced oxidative damage and drive therapy resistance (59, 60). These findings suggest that microglia associated signaling contributes to therapy resistant and survival related adaptations within the GBM microenvironment in our model. On the other hand, reported TMZ sensitivities for U87 cell line vary, with IC_{50} values ranging from 34.1 μM to 650.0 μM (61), thereby limiting translational relevance of drug response studies using standard 2D cultures or immortalized cell lines. A key limitation of the present study is the use of immortalized U87 glioblastoma cell line as cell source. Although widely applied in *in vitro* research, U87 cells do not fully represent the intrinsic characteristics of patient derived GBM tumors (62, 63). This limitation may restrict the translational accuracy of the observed responses, particularly in the context of therapeutic evaluation. Moreover, therapeutic responses in this model were not benchmarked against clinical datasets or patient derived treatment outcomes, which limits assessment of its capacity to predict clinical treatment efficacy. Future studies incorporating patient derived or glioma stem-like cells and correlating model derived drug response data with clinical cohorts will be critical to validate the translational relevance and predictive potential of this platform. Additionally, although the model includes microglia to mimic immune-tumor interactions, it employs the HMC3 cell line, an immortalized human microglial model. While offering human origin, HMC3 cells do not fully reproduce the phenotypic heterogeneity, activation states, or immune regulatory functions exhibited by primary microglia in the native tissue (64, 65). Another limitation of this model is the absence of a blood-brain barrier (BBB) component, which plays a direct role in drug transport and therapeutic response. BBB-like structures have been successfully incorporated into glioblastoma-on-a-chip platforms. For example, Silvani et al. (2021) developed a 3D bioprinted vascularized model that included a perfusable BBB structure and compartmentalized tumor architecture under physiological shear stress (66). Integrating a similar BBB component into future work with this model could strengthen its translational value and usefulness in drug screening. Furthermore, the absence of other critical immune cell populations, such as tumor associated macrophages, T cells, and myeloid derived suppressor cells, restrict the capacity of the platform to capture the immunological complexity of the glioblastoma microenvironment.

View Article Online
DOI: 10.1039/D5BM01824B

Overall, integrating an ECM-like matrix and microglia interaction with oxygen gradients in the model reproduced several key features of GBM, including histopathologic characteristics, invasion, heterogeneity, metabolic adaptation, and resistance to therapy. This platform may offer a useful platform for studying hypoxia related tumor biology and testing therapeutic strategies under conditions that closely resemble the GBM microenvironment. Incorporating patient derived cells, additional immune populations, and advanced molecular analysis into future studies could further improve its capacity to represent GBM complexity and support translational applications.

5. Conclusion

In this study, a bioprinted GBM model combining a PDMS based hypoxia chip, microglia interaction and an ECM mimetic hydrogel was produced. The inclusion of a glass diffusion barrier facilitated the formation of oxygen gradients without requiring external gas control or chemicals. The platform reproduced key pathological features of GBM, including pseudopalisading necrosis, heterogeneity, metabolic adaptation, and chemoresistance. Under hypoxia, cells within the chip exhibited increased proliferation, invasion, and stemness related gene expression, consistent with hypoxia driven reprogramming observed *in vivo*. The model also demonstrated increased resistance to TMZ under hypoxic conditions, indicating the influence of oxygen gradients and extracellular matrix cues on drug response. These findings highlight the importance of mimicking hypoxic conditions, matrix characteristics, and microglia interactions of the tumor microenvironment for *in vitro* modeling. Since the current model uses immortalized cell lines, integration of cancer and immune cells from patients into the future work could enhance its translational value. At present, this hypoxia chip serves as a basis for developing physiologically relevant tools to study GBM progression and evaluate novel therapeutic approaches.

Funding statement

This study was supported by the Scientific and Technological Research Council of Turkey (TUBITAK) through Grant 323S338 and BIDEB 2211-C program, and by the Scientific Research Projects Coordination Unit of Acibadem University under project no 2312.

Conflict of Interest Statement

The authors declared no potential conflicts of interest with respect to the research, authorship, and/or publication of this article.

View Article Online
DOI: 10.1039/D5BM01824B

Ethical Statement

This study did not require ethical approval.

Informed consent

There are no human participants in this study, and informed consent is not required.

Data Availability Statement

The data supporting the findings of this study are available from the corresponding author upon reasonable request.

Acknowledgements

Authors would like to acknowledge the Biomaterials Application and Research Center of Acibadem University for the use of the facilities. We also thank Furkan Şahin for his support during the LC-MS/MS experiments.

References

1. Wen PY, Weller M, Lee EQ, Alexander BM, Barnholtz-Sloan JS, Barthel FP, et al. Glioblastoma in adults: a Society for Neuro-Oncology (SNO) and European Society of Neuro-Oncology (EANO) consensus review on current management and future directions. Neuro-oncology. 2020;22(8):1073-113.
2. Jin X, Kuang Y, Li L, Li H, Zhao T, He Y, et al. A positive feedback circuit comprising p21 and HIF-1α aggravates hypoxia-induced radioresistance of glioblastoma by promoting Glut1/LDHA-mediated glycolysis. The FASEB Journal. 2022;36(3):e22229.
3. Wang P, Gong S, Liao B, Liu J, Zhao L, Wu N. HIF-1α and HIF-2α: synergistic regulation of glioblastoma malignant progression during hypoxia and apparent chemosensitization in response to hyperbaric oxygen. Cancer Cell International. 2025;25(1):251.
4. Ganesh RA, Sonpatki P, Naik D, John AE, Sathe G, Lakshmikantha A, et al. Multi-omics analysis of glioblastoma and glioblastoma cell line: molecular insights into the functional role of GPR56 and TG2 in mesenchymal transition. Frontiers in oncology. 2022;12:841890.
5. Marallano VJ, Ughetta ME, Tejero R, Nanda S, Ramalingam R, Stalbow L, et al. Hypoxia drives shared and distinct transcriptomic changes in two invasive glioma stem cell lines. Scientific Reports. 2024;14(1):7246.
6. Greenwald AC, Darnell NG, Hoefflin R, Simkin D, Mount CW, Gonzalez Castro LN, et al. Integrative spatial analysis reveals a multi-layered organization of glioblastoma. Cell. 2024;187(10):2485-501 e26.
7. Ramos-Fresnedo A, Domingo RA, Perez-Vega C, Pullen MW, Akinduro OO, Almeida JP, et al. The early infiltrative phase of GBM hypothesis: are molecular glioblastomas histological glioblastomas in the making? A preliminary multicenter study. Journal of neuro-oncology. 2022;158(3):497-506.
8. Bikfalvi A, da Costa CA, Avril T, Barnier J-V, Bauchet L, Brisson L, et al. Challenges in glioblastoma research: focus on the tumor microenvironment. Trends in cancer. 2023;9(1):9-27.
9. Torrisi F, Alberghina C, D'Aprile S, Pavone AM, Longhitano L, Giallongo S, et al. The hallmarks of glioblastoma: heterogeneity, intercellular crosstalk and molecular signature of invasiveness and progression. Biomedicines. 2022;10(4):806.
10. Bayona C, Alza L, Ranđelović T, Sallán MC, Visa A, Cantí C, et al. Tetralol derivative NNC-55-0396 targets hypoxic cells in the glioblastoma microenvironment: an organ-on-chip approach. Cell Death & Disease. 2024;15(2):127.
11. Oh JM, Begum HM, Liu YL, Ren Y, Shen K. Recapitulating tumor hypoxia in a cleanroom-free, liquid-pinning-based microfluidic tumor model. ACS biomaterials science & engineering. 2022;8(7):3107-21.

DOI: 10.1039/D5BM01824B

12. Yi HG, Jeong YH, Kim Y, Choi YJ, Moon HE, Park SH, et al. A bioprinted human-glioblastoma-on-a-chip for the identification of patient-specific responses to chemoradiotherapy. Nat Biomed Eng. 2019;3(7):509-19.

13. Refet-Mollof E, Najyb O, Chermat R, Glory A, Lafontaine J, Wong P, et al. Hypoxic jumbo spheroids on-A-chip (HOnAChip): insights into treatment efficacy. Cancers. 2021;13(16):4046.

14. Wang C, Zhao Q, Zheng X, Li S, Chen J, Zhao H, et al. Decellularized brain extracellular matrix slice glioblastoma culture model recapitulates the interaction between cells and the extracellular matrix without a nutrient-oxygen gradient interference. Acta Biomaterialia. 2023;158:132-50.

15. Smith LJ, Skirzynska A, Chin AA, Arnold AE, Kushida M, Dirks PB, et al. Engineered in vitro tumor model recapitulates molecular signatures of invasion in glioblastoma. ACS Materials Au. 2023;3(5):514-27.

16. Heinrich MA, Bansal R, Lammers T, Zhang YS, Michel Schiffelers R, Prakash J. 3D-bioprinted mini-brain: a glioblastoma model to study cellular interactions and therapeutics. Advanced materials. 2019;31(14):1806590.

17. Tang M, Xie Q, Gimple RC, Zhong Z, Tam T, Tian J, et al. Three-dimensional bioprinted glioblastoma microenvironments model cellular dependencies and immune interactions. Cell Res. 2020;30(10):833-53.

18. Chen J-WE, Lumibao J, Leary S, Sarkaria JN, Steelman AJ, Gaskins HR, et al. Crosstalk between microglia and patient-derived glioblastoma cells inhibit invasion in a three-dimensional gelatin hydrogel model. Journal of neuroinflammation. 2020;17(1):346.

19. Isik S, Yucel D, Hasirci V. Development of a Hydrogel Platform with GBM and Microglia: A Potential Glioblastoma Tumor Model. ACS Applied Bio Materials. 2025.

20. Antmen E, Demirci U, Hasirci V. Micropatterned Surfaces Expose the Coupling between Actin Cytoskeleton-Lamin/Nesprin and Nuclear Deformability of Breast Cancer Cells with Different Malignancies. Advanced biology. 2021;5(1):2000048.

21. Ayuso JM, Monge R, Martínez-González A, Virumbrales-Muñoz M, Llamazares GA, Berganzo J, et al. Glioblastoma on a microfluidic chip: Generating pseudopalisades and enhancing aggressiveness through blood vessel obstruction events. Neuro-oncology. 2017;19(4):503-13.

22. Wu Y, Clark KC, Nguyen EV, Niranjan B, Horvath LG, Taylor RA, et al. Proteomic characterisation of prostate cancer intercellular communication reveals cell type-selective signalling and TMSB4X-dependent fibroblast reprogramming. Cellular Oncology. 2022;45(6):1311-28.

23. Kolde R. pheatmap: Pretty Heatmaps. R package version 1.0.13; 2025. Available from: https://CRAN.R-project.org/package=pheatmap.

24. Wickham H. ggplot2: Elegant Graphics for Data Analysis; Springer-Verlag: New York, 2016.

25. R Core Team. R: A Language and Environment for Statistical Computing; R Foundation for Statistical Computing: Vienna, Austria, 2026. https://www.R-project.org/.

26. Amorim P, d'Ávila M, Anand R, Moldenaers P, Van Puyvelde P, Bloemen V. Insights on shear rheology of inks for extrusion-based 3D bioprinting. Bioprinting. 2021;22:e00129.

27. Elango J, Zamora-Ledezma C. Rheological, structural, and biological trade-offs in bioink design for 3d bioprinting. Gels. 2025;11(8):659.

28. Tang M, Tiwari SK, Agrawal K, Tan M, Dang J, Tam T, et al. Rapid 3D Bioprinting of Glioblastoma Model Mimicking Native Biophysical Heterogeneity. Small. 2021;17(15):e2006050.

29. Comba A, Faisal SM, Dunn PJ, Argento AE, Hollon TC, Al-Holou WN, et al. Spatiotemporal analysis of glioma heterogeneity reveals COL1A1 as an actionable target to disrupt tumor progression. Nature communications. 2022;13(1):3606.

30. Chédeville AL, Lourdusamy A, Monteiro AR, Hill R, Madureira PA. Investigating glioblastoma response to hypoxia. Biomedicines. 2020;8(9):310.

31. Stanke KM, Wilson C, Kidambi S. High expression of glycolytic genes in clinical glioblastoma patients correlates with lower survival. Frontiers in Molecular Biosciences. 2021;8:752404.

32. D'Aprile S, Denaro S, Gervasi A, Vicario N, Parenti R. Targeting metabolic reprogramming in glioblastoma as a new strategy to overcome therapy resistance. Frontiers in Cell and Developmental Biology. 2025;13:1535073.

33. Wei R, Zhou J, Bui B, Liu X. Glioma actively orchestrate a self-advantageous extracellular matrix to promote recurrence and progression. BMC cancer. 2024;24(1):974.

View Article Online
DOI: 10.1039/D5BM01824B

34. Zhang G, Tao X, Ji B, Gong J. Hypoxia-driven M2-polarized macrophages facilitate cancer aggressiveness and temozolomide resistance in glioblastoma. Oxidative Medicine and Cellular Longevity. 2022;2022(1):1614336.

35. Feldman L. Hypoxia within the glioblastoma tumor microenvironment: a master saboteur of novel treatments. Frontiers in immunology. 2024;15:1384249.

36. Palacio-Castañeda V, Kooijman L, Venzac B, Verdurmen WP, Le Gac S. Metabolic switching of tumor cells under hypoxic conditions in a tumor-on-a-chip model. Micromachines. 2020;11(4):382.

37. Abd Elmaogod EA, Daoud SA, Mostafa ZM, Mahmoud EMM. Prognostic significance of HIF1-α immunohistochemical expression in gliomas and it's relation to IDH1 mutation status. Beni-Suef University Journal of Basic and Applied Sciences. 2022;11(1):140.

38. Liu D, Wan Y, Qu N, Fu Q, Liang C, Zeng L, et al. LncRNA-FAM66C was identified as a key regulator for modulating tumor microenvironment and hypoxia-related pathways in glioblastoma. Frontiers in public health. 2022;10:898270.

39. Macharia LW, Muriithi W, Nyaga DK, de Mattos Coelho-Aguiar J, de Sampaio e Spohr TCL, Moura-Neto V. Evaluation of MiRNA Expression in Glioblastoma Stem-Like Cells: A Comparison between Normoxia and Hypoxia Microenvironment. Onco. 2022;2(2):113-28.

40. Macharia LW, Muriithi W, Heming CP, Nyaga DK, Aran V, Mureithi MW, et al. The genotypic and phenotypic impact of hypoxia microenvironment on glioblastoma cell lines. BMC cancer. 2021;21(1):1248.

41. Shah N, Hallur PM, Ganesh RA, Sonpatki P, Naik D, Chandrachari KP, et al. Gelatin methacrylate hydrogels culture model for glioblastoma cells enriches for mesenchymal-like state and models interactions with immune cells. Scientific reports. 2021;11(1):17727.

42. Kim Y, Varn FS, Park S-H, Yoon BW, Park HR, Lee C, et al. Perspective of mesenchymal transformation in glioblastoma. Acta neuropathologica communications. 2021;9(1):50.

43. Mathur R, Wang Q, Schupp PG, Nikolic A, Hilz S, Hong C, et al. Glioblastoma evolution and heterogeneity from a 3D whole-tumor perspective. Cell. 2024;187(2):446-63. e16.

44. Tribe AK, McConnell MJ, Teesdale-Spittle PH. The big picture of glioblastoma malignancy: A meta-analysis of glioblastoma proteomics to identify altered biological pathways. ACS omega. 2021;6(38):24535-44.

45. Reuss AM, Groos D, Buchfelder M, Savaskan N. The acidic brain—glycolytic switch in the microenvironment of malignant glioma. International journal of molecular sciences. 2021;22(11):5518.

46. Jacquet P, Stéphanou A. Beyond the Warburg Effect: Modeling the Dynamic and Context-Dependent Nature of Tumor Metabolism. Cancers. 2025;17(21):3563.

47. Xie X, Zhou W, Ku Y, Li S, Yang Y, Hao X, et al. Lactate-Mediated Epigenetic and Immunometabolic Reprogramming in Glioma: An Emerging Axis Linking Metabolism to Tumor Progression. Biomedicines. 2025;13(12):3041.

48. Gao Y, Zhang M, Wang G, Lai W, Liao S, Chen Y, et al. Metabolic cross-talk between glioblastoma and glioblastoma-associated microglia/macrophages: from basic insights to therapeutic strategies. Critical Reviews in Oncology/Hematology. 2025;208:104649.

49. Nishikawa M, Inoue A, Ohnishi T, Yano H, Ozaki S, Kanemura Y, et al. Hypoxia-induced phenotypic transition from highly invasive to less invasive tumors in glioma stem-like cells: Significance of CD44 and osteopontin as therapeutic targets in glioblastoma. Translational oncology. 2021;14(8):101137.

50. Djediai S, Gonzalez Suarez N, El Cheikh-Hussein L, Rodriguez Torres S, Gresseau L, Dhayne S, et al. MT1-MMP cooperates with TGF-β receptor-mediated signaling to trigger SNAIL and induce epithelial-to-mesenchymal-like transition in U87 glioblastoma cells. International Journal of Molecular Sciences. 2021;22(23):13006.

51. Joseph JV, Conroy S, Pavlov K, Sontakke P, Tomar T, Eggens-Meijer E, et al. Hypoxia enhances migration and invasion in glioblastoma by promoting a mesenchymal shift mediated by the HIF1α–ZEB1 axis. Cancer letters. 2015;359(1):107-16.

52. Parihar K, Nukpezah J, Iwamoto DV, Cruz K, Byfield FJ, Chin L, et al. Tissue-dependent mechanosensing by cells derived from human tumors. npj Biological Physics and Mechanics. 2025;2(1):19.

View Article Online
DOI: 10.1039/D5BM01824B

53. Vedarethinam V, Mayakrishnan V, Mani RR, Chang SW, Ravindran B. Integrative diagnostics of cancer's extracellular matrix: Synergizing imaging and multi-omics for precision medicine. Journal of Radiation Research and Applied Sciences. 2025;18(3):101636.
54. Tian Y, Cheng T, Sun F, Zhou Y, Yuan C, Guo Z, et al. Effect of biophysical properties of tumor extracellular matrix on intratumoral fate of nanoparticles: Implications on the design of nanomedicine. Advances in Colloid and Interface Science. 2024:103124.
55. Ge X, Pan M-H, Wang L, Li W, Jiang C, He J, et al. Hypoxia-mediated mitochondria apoptosis inhibition induces temozolomide treatment resistance through miR-26a/Bad/Bax axis. Cell death & disease. 2018;9(11):1128.
56. Musah-Eroje A, Watson S. A novel 3D in vitro model of glioblastoma reveals resistance to temozolomide which was potentiated by hypoxia. Journal of Neuro-oncology. 2019;142(2):231-40.
57. Sørensen MD, Olsen RFS, Burton M, Kavan S, Petterson SA, Thomassen M, et al. Microglia induce an interferon-stimulated gene expression profile in glioblastoma and increase glioblastoma resistance to temozolomide. Neuropathology and Applied Neurobiology. 2024;50(6):e13016.
58. Solomou G, Young AM, Bulstrode HJ. Microglia and macrophages in glioblastoma: landscapes and treatment directions. Molecular Oncology. 2024;18(12):2906-26.
59. Campos-Sandoval JA, Gómez-García MC, de Los Santos-Jiménez J, Matés JM, Alonso FJ, Márquez J. Antioxidant responses related to temozolomide resistance in glioblastoma. Neurochemistry international. 2021;149:105136.
60. Nowacka A, Śniegocki M, Ziółkowska E. Oxidative stress and antioxidants in glioblastoma: mechanisms of action, therapeutic effects and future directions. Antioxidants. 2025;14(9):1121.
61. Poon MT, Bruce M, Simpson JE, Hannan CJ, Brennan PM. Temozolomide sensitivity of malignant glioma cell lines–a systematic review assessing consistencies between in vitro studies. BMC cancer. 2021;21:1-9.
62. Allen M, Bjerke M, Edlund H, Nelander S, Westermark B. Origin of the U87MG glioma cell line: Good news and bad news. Science translational medicine. 2016;8(354):354re3-re3.
63. Schulz JA, Rodgers LT, Kryscio RJ, Hartz AM, Bauer B. Characterization and comparison of human glioblastoma models. BMC cancer. 2022;22(1):844.
64. Dello Russo C, Cappoli N, Coletta I, Mezzogori D, Paciello F, Pozzoli G, et al. The human microglial HMC3 cell line: where do we stand? A systematic literature review. Journal of neuroinflammation. 2018;15(1):259.
65. Gunasegaran B, Krishnamurthy S, Chow SS, Villanueva MD, Guller A, Ahn SB, et al. Comparative analysis of HMC3 and C20 microglial cell lines reveals differential myeloid characteristics and responses to immune stimuli. Immunology. 2025;175(1):84-102.
66. Silvani G, Basirun C, Wu H, Mehner C, Poole K, Bradbury P, et al. A 3D-Bioprinted Vascularized Glioblastoma-on-a-Chip for Studying the Impact of Simulated Microgravity as a Novel Pre-Clinical Approach in Brain Tumor Therapy. Advanced Therapeutics. 2021;4(11).

View Article Online
DOI: 10.1039/D5BM01824B

Data Availability Statement

The data supporting the findings of this study are available from the corresponding author upon reasonable request.